



Vera C. Rubin Observatory
Rubin Observatory Operations

Study of the Photon Transfer Curve in the CCD detectors of the Vera C. Rubin Observatory

Lina M. Giraldo Murillo, Jerónimo Calderon,
Andrés A. Plazas Malagón, and Craig S. Lage

RTN-056

<https://doi.org/10.71929/rubin/2575156>

Latest Revision: 2025-08-08



Abstract

The RECA internship program provides Colombian students with an opportunity to enhance their research skills in Astronomy, Astrophysics, and Cosmology. During this three-month program, our main objective was to study the Photon Transfer Curves (PTC) of the Vera C. Rubin Observatory, specifically the gain, and to compare it with the gain obtained through pairs of flats.

Overall, the study of PTCs is crucial in understanding the performance of detectors and instruments used in Astronomy. The Vera C. Rubin Observatory is an important facility that will enable researchers to carry out a wide range of studies in this field, making it essential to investigate its gain performance.

We used run 13144 to construct the PTCs and 13186 to analyze the crosstalk. We employed the LSST Science Pipelines (also known as the *DM stack*), a software under development for this observatory, which performs all the necessary reductions for the construction of the PTCs. We also used simulations to replicate the observed effects.

Initially, we found a 5% difference between the gain calculated by PTC and pairs of flats for a flow range between 5000 and 10000 ADU. Simulations showed that this difference was due to the handling of statistics and the assumption that the distribution following the Lupton equation is Gaussian. We found an error interval for this flow region based on the vendor, with $(1.8 \pm 0.7, 4.1 \pm 0.9) \%$ for E2V and $(0.85 \pm 0.7, 2.2 \pm 0.9) \%$ for ITL. From the PTC, we also obtained the average Full Well Capacity of *LSSTCam* as $130000 \pm 10000 e^-$.

We identified a list of segments where we found differences with the results obtained by SLAC National Acceleration Laboratory in PTC parameters, low saturation level, or other defects. We detected and corrected the effect of statistics in the gain calculation using pairs of flats and proposed a code change, which was implemented in the pipeline software. We do not recommend correcting for crosstalk as it does not significantly affect the parameters and does not change the shape of the PTC. However, the opposite is true for the nonlinearity correction.

Change Record

Version	Date	Description	Owner name
1	YYYY-MM-DD	Unreleased.	Lina Giraldo

Document source location: <https://github.com/lsst/rtn-056>

Contents

1 Introduction	1
1.1 LSST Scientific Goals	1
1.2 CCD Type in LSST Camera	2
1.3 What is Photon Transfer Curve (PTC)?	3
1.3.1 Brighter father effect	5
2 Data	6
3 Methodology	7
3.1 Photon Transfer Curve (PTC)	9
3.2 Gain from flat pairs	10
3.2.1 Simulation	11
3.3 No linearity Correction	15
3.4 Crosstalk Correction	16
4 Results	17
4.1 Photon Transfer Curve	18
4.2 Gain from Flat Pairs	24
4.2.1 Simulation	25
4.2.2 Contrasting the simulations with real data	27
4.3 Crosstalk and Nonlinearity Correction	30
5 Conclusions	34
6 Acknowledgments	35
A References	36
B Acronyms	38

Study of the Photon Transfer Curve in the CCD detectors of the Vera C. Rubin Observatory

1 Introduction

The Vera C. Rubin Observatory is located at Cerro Pachón in the Atacama Desert in Chile. It was selected after careful consideration of various sites worldwide based on their meteorological conditions (Sebag et al., 2006). The observatory will operate the 8.4-meter Simonyi Survey Telescope, which has the capability to scan the entire southern sky in approximately three nights and is expected to start operations in 2024. Additionally, the observatory houses the LSST Camera, the largest camera ever built, with a 3.2 gigapixel resolution for the entire focal plane (SLAC National Accelerator Laboratory & NSF-DOE Vera C. Rubin Observatory, 2025). The LSST Camera has a diameter of 64 cm, covering a 9.6 deg^2 field of view, and a plate scale of $0.2'' \text{ pixel}^{-1}$.

The observatory is named in honor of the renowned astronomer Vera Rubin (NSF, 2020), who, in 1970, pioneered the measurement of the rotation curves of disk galaxies (Rubin, 2011). Her groundbreaking work revealed that there must be more mass than what is observed in galaxies in order for stars to rotate at the observed rate without breaking apart. This additional mass is now known as dark matter, and studying it is one of the scientific goals of the Vera C. Rubin Observatory.

Vera Rubin received numerous awards for her contributions to astronomy, including the National Medal of Science, and even has a ridge on Mars named after her (Koren, 2020). In addition, she was a staunch advocate for recognizing the work of women in science and her students (Rubin, 2011).

1.1 LSST Scientific Goals

The Legacy Survey of Space and Time (formerly Large Synoptic Survey Telescope, LSST) has four primary scientific objectives (LSST Science Collaboration et al., 2009; Ivezić et al., 2019):

- Inventory of the Solar System: The LSST aims to study minor bodies in the solar system,

including Trans-Neptunian Objects (TNOs), asteroids, and comets, to better understand planetary formation and evolution. By analyzing their orbital elements and sizes, the LSST will provide valuable insights into the history of these objects. Additionally, studying the interaction of objects in the Main Asteroid Belt, located between Mars and Jupiter, could shed light on the origin of Near-Earth Objects (NEOs) that come from the Main Belt and enter Earth's orbit.

- **Mapping the Milky Way:** This objective involves studying the structure, dynamics, and chemical composition of stars in our galaxy, the Milky Way, to understand its formation and evolution. The LSST will also characterize stars in the solar neighborhood within 300 parsecs.
- **Exploring the Transient Optical Sky:** The LSST will conduct time-domain science to observe transient and variable phenomena such as supernovae, variable stars, and Active Galactic Nuclei (AGN). The goal is to detect and study transient and distant objects, which requires observing a large portion of the sky to increase the probability of capturing such events, obtaining high-quality images to discern differences between images, capturing data with good sampling time to detect various types of variable stars, obtaining accurate color information for classification, conducting long-term persistent observations to track the events, and processing, classifying, and rapidly publishing data for the community to enable further studies such as spectroscopy.
- **Probing Dark Energy and Dark Matter:** Dark energy, which affects the expansion of the universe, and dark matter, which accumulates mass, can be studied using various mechanisms. The LSST will utilize techniques such as weak gravitational lensing, the study of large-scale structures like galaxy clusters, Baryonic Acoustic Oscillations (BAO), and Supernova systems, among others, to probe dark energy. For the study of dark matter, the LSST will explore weak and strong lensing of galaxy mass distributions, among other approaches.

1.2 CCD Type in LSST Camera

The LSSTCam utilizes *thick fully depleted* and back-illuminated CCDs (SLAC National Accelerator Laboratory & NSF-DOE Vera C. Rubin Observatory, 2025). These CCDs are known for their excellent response in the near-infrared regions (Lage et al., 2017), making them suitable for observing distant objects that are reddened by the universe's expansion. However, due to

their thickness, they can exhibit effects caused by the long path that electrons must travel to the charge storage well.

Highly segmented, the LSSTCam can be read out completely in 2 seconds, reducing the readout noise associated with high readout speeds (LSST Science Collaboration et al., 2009). It consists of a mosaic of 205 CCDs organized into 21 science modules, each containing nine CCDs, along with four specialized corner modules for telescope guidance and alignment through active optics (Snyder et al., 2020). The CCDs in the mosaic are sourced from two vendors: Imaging Technology Laboratories (ITL) and Teledyne e2v (E2V), with each CCD divided into 16 segments. Figure 1 illustrates the ITL detectors in greenish blue, the E2V detectors in yellow, which are used for science, and the guidance CCDs in purple.

As mentioned by Walter (2015), precise measurements of the point spread function (PSF) of galaxies are essential for the LSST's science objective in weak lensing, where the goal is to study how the shape of galaxies is modified by observing a wide field. To achieve this, it is crucial to quantify the brighter-fatter (BF) effect, which causes deformation of the PSF and is more significant in brighter objects, gradually decreasing in fainter objects (Lage et al., 2017). Additionally, Walter (2015) notes that the sensors also experience an edge effect, where electrons near the edge of the sensor feel a force that pushes them inward, primarily affecting astrometry.

1.3 What is Photon Transfer Curve (PTC)?

The Photon Transfer Curve (PTC) is a characterization tool used to determine the fundamental parameters of a CCD, such as the gain, which represents the relationship between the electrons recorded by each pixel and their conversion to Analog-to-Digital Unit (ADU). The PTC also measures the nonlinearity of the camera and its Full Well Capacity (FWC). The gain is a crucial parameter as it impacts other vital parameters like read noise, quantum efficiency, dark current, and more, making it essential for a comprehensive understanding of CCD performance (Downing et al., 2006).

Figure 2 shows the PTC of segment C06 of sensor 22 of the LSSTCam. It is evident that at low fluxes, the variance is low and increases with the flux, but not linearly, until reaching the saturation point or FWC, which is 83000 ADU for this detector. Beyond this point, the variance begins to decrease, indicating that the flux stored in each pixel of this amplifier starts

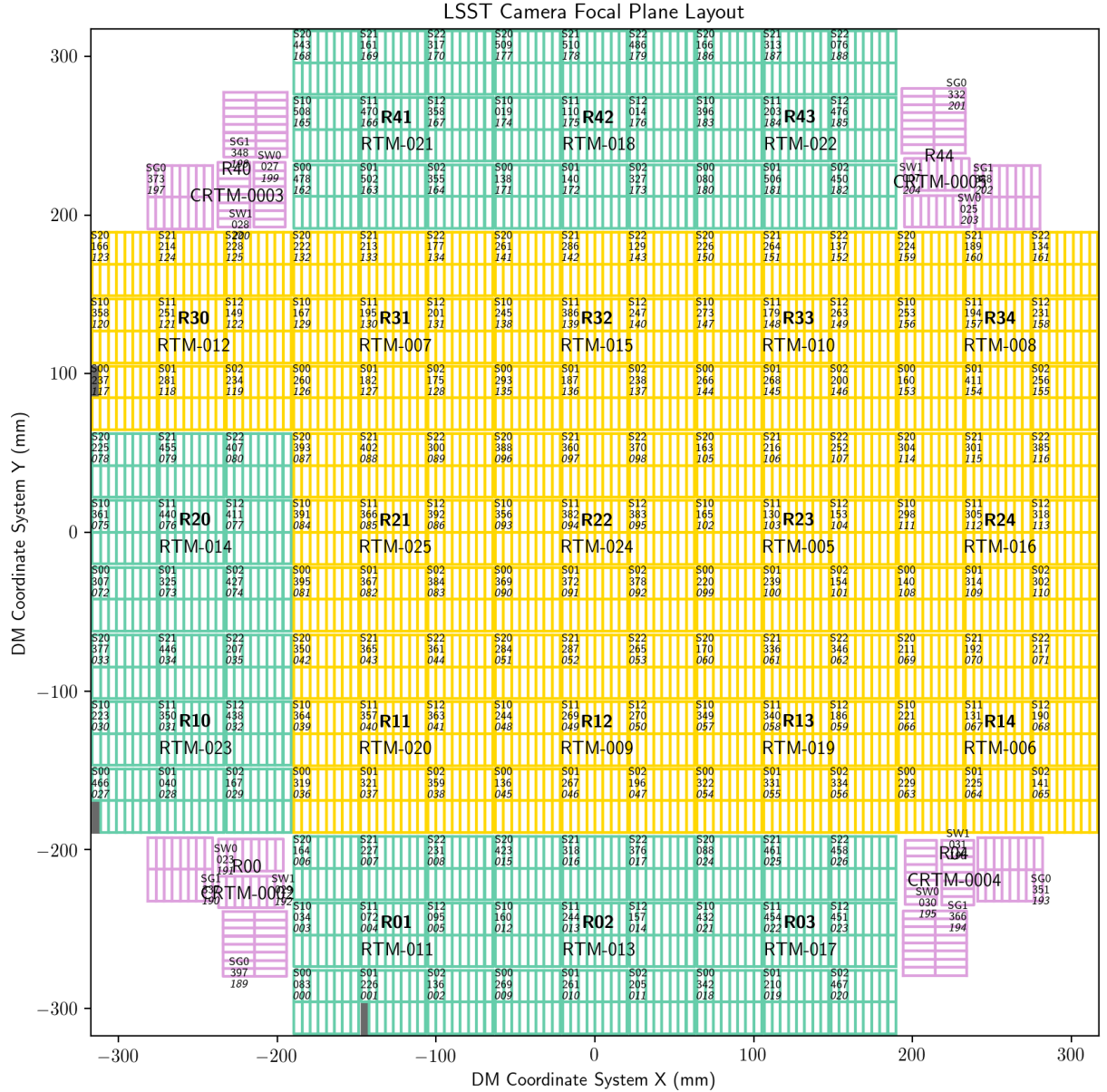


Figure 1: The focal plane of the LSST camera. The vendor's CCDs' location is blue for ITL and yellow for E2V. Each CCD (a small square) is composed of 16 segments, each with its amplifier, and 189 CCDs are responsible for taking the science data. The CCDs at the corners are for focusing and synchronization with the Earth's rotation (see LSST-SLACLab). *Image credits: Seth Digel/LSST Camera project.*

to homogenize. This nonlinear behavior is exhibited by *thick fully-depleted CCDs* as explained by Downing et al. (2006), where charge storage in a pixel is the main cause for the deviation from the expected relationship between variance and mean number of counts in a pixel, es-

pecially in flat images (Walter, 2015). The effective area of the pixel changes with the amount of charge, decreasing as the charge accumulated in the pixel increases. As a result, very bright sources are mainly affected by this phenomenon known as the BF effect. If the pixels of the CCD segment were independent, they could be described by Poisson statistics, and the PTC would follow the green line in the figure.

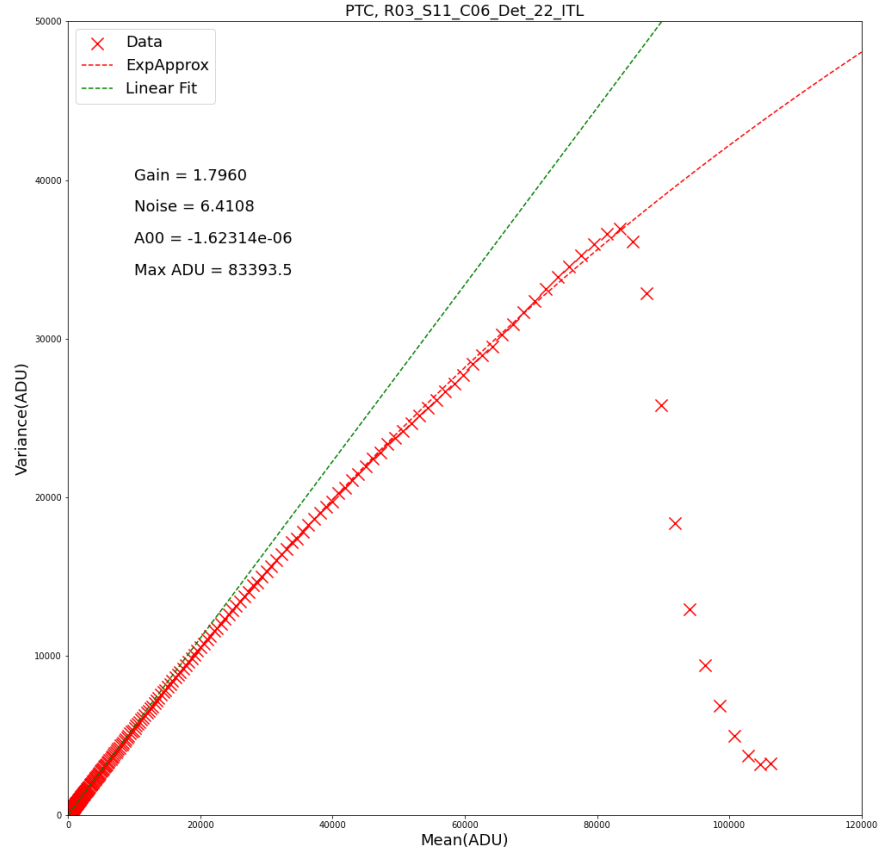


Figure 2: Photon Transfer Curve (PTC) for detector 22, which is located in raft 03, sensor 11, and amplifier C06, and manufactured by ITL. The red crosses represent the data points, the red line shows the EXPAPPROXIMATION fit, and the green line represents the linear fit. This PTC curve was generated using the results obtained via the *DM stack*.

1.3.1 Brighther father effect

As mentioned previously, the charge stored in a pixel can alter the effective area of the pixel, reducing the probability that the pixel will continue to store the charge. This can result in horizontal deflection of the electrons, causing more elliptical images. This phenomenon breaks down the initial assumption of Poisson statistics and independent charge storage in each pixel, thereby modifying the relationship between the variance and the mean number of

counts per pixel (Walter, 2015). This effect can impact the Point Spread Function (PSF) and may pose a potential problem for surveys that are interested in studying variations in brightness and shape of objects (Coulton et al., 2018).

This work was conducted during the RECA (Red de Estudiantes Colombiana de Astronomía) internship program in 2022¹. The program spanned three months and also involved other activities such as remote astronomical observations at the Teide Observatory².

In this report, we present the data used in Section 2, describe the methodology in Section 3, present the results and analysis in Section 4, and provide conclusions in Section 5."

2 Data

The data used in this study were obtained using the Bench for Optical Testing (BOT), which was constructed and designed at SLAC National Accelerator Laboratory. The BOT enables laboratory tests with the LSSTCam, ensuring that flat images exhibit variations of less than 5% for accurate measurements of linearity, FWC, and gain from the PTCs (Newbry et al., 2018). Figure 3 illustrates the structure of the BOT, with the cryostat located at the circular top and the focal plane pointing downwards on the test bench.

The data for this study were obtained from *run 13144* and *run 13186*, with the latter containing the crosstalk matrix information. As described in Snyder et al. (2020), electronic crosstalk measurements were conducted using a projector known as the *crosstalk projector*, which illuminates a single sensor with a collimated beam of light with a pattern containing large bright spots, each with a radius of 80 pixels. However, for laboratory tests simulating realistic source sizes, the *spot grid projector*, an optical projector, was used. This projector generates spots in specific grids and includes filters to simulate both satellite trails and the signal level of the sky background.

¹The RECA internship program is a scientific research training program in Astronomy, Astrophysics, and Cosmology for students from Colombian institutions. Program website: <https://recastronomia.github.io/internship/>

²<https://www.iac.es/es/observatorios-de-canarias/observatorio-del-teide>

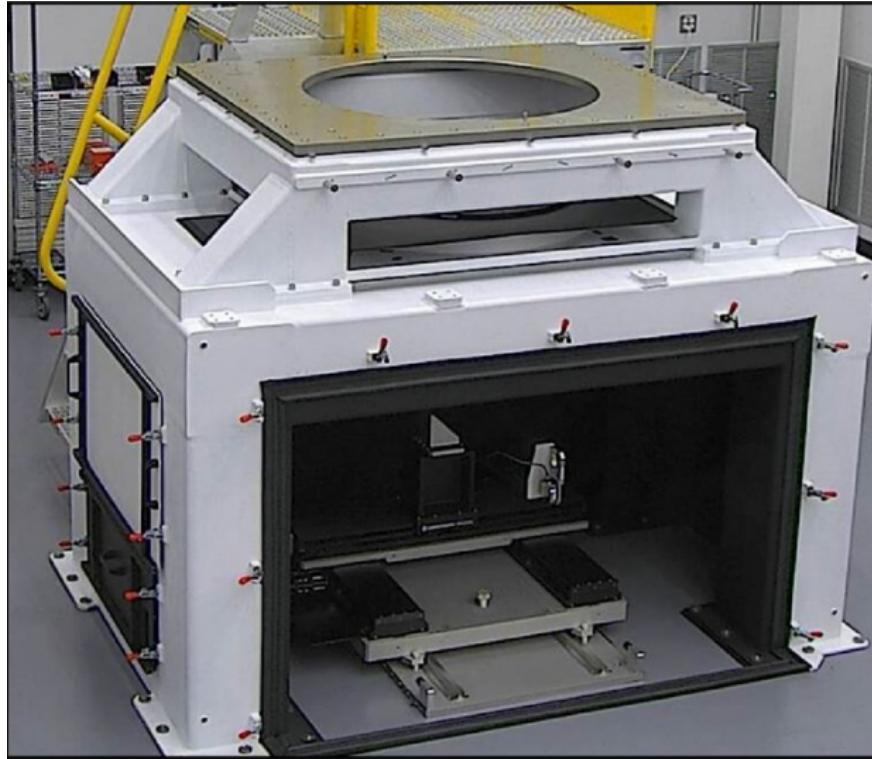


Figure 3: Bench for Optical Testing (BOT) designed by SLAC. Figure is taken from Newbry et al. (2018).

3 Methodology

The images used in this study underwent standard reduction techniques, including overscan, bias, dark, and defects reduction. Defects reduction involves creating maps that indicate regions with both bright and dark defects, such as dead pixels. These reductions serve as the starting state for the PTC study. Subsequently, other corrections, such as linearity and crosstalk, are applied to analyze their effects on the main parameters of the camera.

Professor Craig Lage generated supercalibrations for the entire focal plane, which are stored in his personal collection at [u/cslage/calib/13144/calib.20220103](https://github.com/cslage/calib/13144/calib.20220103). The images shown in Figures 4 and 5 are superbias and superdarks, respectively, generated as part of the learning process for producing the calibration images using the LSST's software called *DM stack* [PSTN-019].

The code used to generate the calibration images via *DM stack* can be found at https://github.com/lsst/cp_pipe. This code generates the data for the construction of the PTC

and calculates the gain for each CCD segment as its FWC. Additionally, it calculates the gain using another method, which was analyzed in Section 3.2 to determine the differences between it and the PTC method. The alternative method involves using two pairs of flats for gain estimation. We utilized two versions of the *DM stack* code³ for the entire focal plane:

- w_2022_27: Initial version we started working with.
- w_20222_32: Version that includes one of our main results on obtaining the gain with pairs of flats (see the DM-35790 ticket in Jira).

BPS (Batch Processing Service) was utilized to run the two previous versions. Detailed instructions on how to build the configuration files, handle possible errors, and access more information can be found in the GitHub repository of this project, RECA_Internship_Project, in the notebook BPS_LSST.ipynb. Additionally, all the notebooks used to carry out the methodology described below are available in this repository. There is also a tutorial notebook called Tutorial.ipynb, where I provide an overview of the *Data Butler*, the API that manages and stores the data. It includes information on collections, image visualization, data retrieval, and other details related to the calibration images.

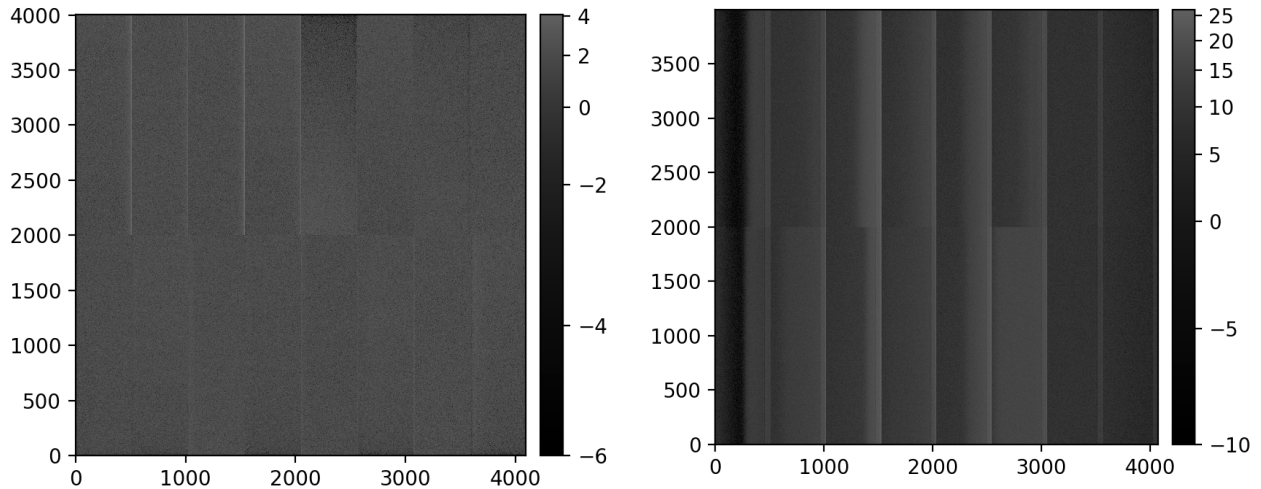


Figure 4: Masterbias images for detectors 55 (E2V) on the left and 74 (ITL) on the right.

³The DM stack software is developed for the LSST and is publicly available on GitHub at <https://github.com/lsst/>

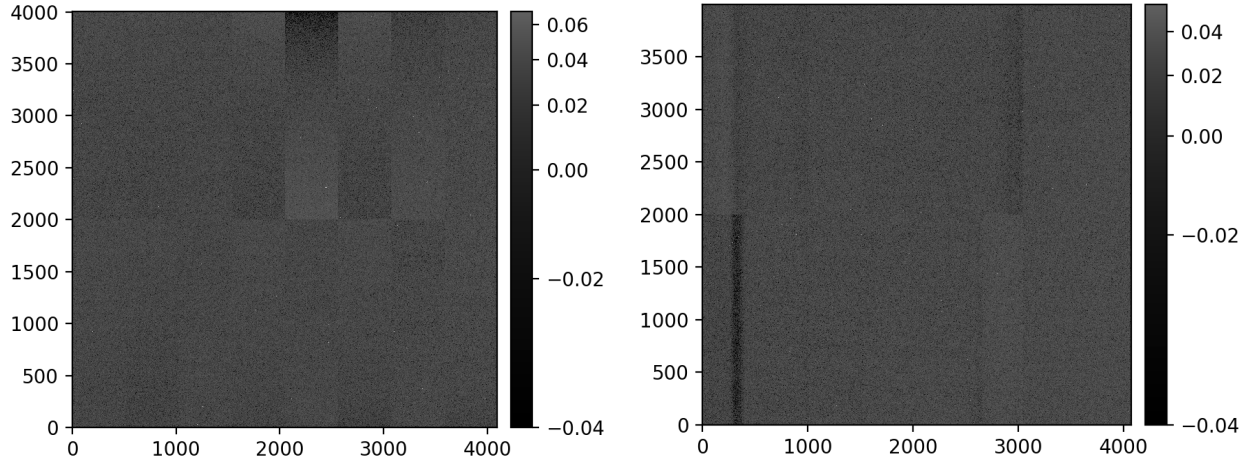


Figure 5: Masterdarks images for detectors 55 (E2V) on the left and 74 (ITL) on the right

3.1 Photon Transfer Curve (PTC)

The PTCs were generated for the entire LSSTCam focal plane using the *DM stack*⁴, which allows estimating the gain, read noise, a_{00} (parameter related to the BF effect), and turnoff (associated with the FWC) from a fit to the shape of the PTC. This code implements equations 16 and 20 of the Astier et al. (2019) article: equation 16 corresponds to the exponential approximation (EXPAPPROXIMATION), which uses only the variance (C_{00}); while equation 20 is the full model (FULLCOVARIANCE), and implements the covariance matrix. In this work, we used EXPAPPROXIMATION, which is described by the following equation:

$$C_{00} = \frac{1}{2g^2a_{00}}[\exp(2a_{00}\mu g) - 1] + \frac{n_{00}}{g^2} \quad (1)$$

where C_{00} is the variance, g is the gain, a_{00} is always negative and is related to the B-F effect, μ is the mean, and n_{00} (el^2) is the noise. According to Astier et al. (2019), a negative value of a_{00} leads to the variance of a flat field not growing as fast as the mean does. In the case where there is no BF effect, i.e., each pixel is independent of the other and is described by a Poisson statistic, the mean, gain, and variance are directly related through the equation:

$$V = \frac{\mu}{g} \quad (2)$$

⁴The PTCs are constructed with the code available in the repository `cp_pipe`

where V is the variance of a flat field, μ is the mean, and g is the gain.

3.2 Gain from flat pairs

An independent method for calculating a sensor's gain is using flat field pairs with equal exposure times. Since each CCD is composed of 16 segments, each with its amplifier, a gain value is obtained for each segment. For this purpose, LSST has the function Gain from flat pairs, which was analyzed in detail in this work.

We aim to quantify the difference between the gain calculated from the fit to the PTC and this independent method using flat field pairs with equal exposure times. For this, we initially calculate the average flux in ADU with each flat pair, the read noise, and the gain. The latter is estimated employing the equation of Lupton (2014):

$$\frac{1}{g} = \left\langle \frac{(I_1 - I_2)^2}{I_1 + I_2} \right\rangle \quad (3)$$

where g is the gain, I_1 is the first flat image, and I_2 is the second flat image, both taken at the same exposure time. The expected value over all pixels is the inverse of the gain. Considering corrections for read-out noise, the equation takes the following quadratic form:

$$\frac{1}{g} = \left\langle \frac{(I_1 - I_2)^2}{I_1 + I_2} \right\rangle - \frac{1}{\mu} (N^2 - \frac{1}{2}g^2) \quad (4)$$

Where $\mu = 0.5(\mu_1 + \mu_2)$, with μ_1 and μ_2 being the average values for each of the flat images, and N is the read-out noise. The equation above has three variants: NONE, SIMPLE, and FULL, with NONE being equivalent to Equation 3. The remaining two cases are as follows:

$$g = \begin{cases} \frac{1}{K - \frac{1}{\mu}(N^2 - \frac{1}{2}g^2)} & \text{SIMPLE} \\ \frac{\mu + \sqrt{\mu^2 - 2\mu K + 2N^2}}{2K\mu - 2K^2} & \text{FULL} \end{cases} \quad (5)$$

where K is equal to Equation 3. In the SIMPLE case, $g = 1/K$, while in the FULL case, the quadratic equation is solved, and the result is taken to have physical meaning. Once we have the gains calculated from pairs of flats for flows between 0 and ~ 10000 ADU, we calculate the relative percentage error with the gain obtained from the fit to the PTC using Equation 5 with the FULL type correction:

$$\text{Relative_error}[\%] = \frac{|gain_{PTC} - gain_{flats}|}{gain_{PTC}} \times 100\% \quad (6)$$

Subsequently, a linear low-flow fit was performed, which we considered to be between 5000 and 10000 ADU. The low-flow fit has the following form:

$$\text{Relative_error}_{LF}[\%] = mF + \text{offset} \quad (7)$$

Where m is the slope of the fit, F is the flux, and offset is the intercept with the y -axis. These parameters are used to quantify the error variation in the specified flow range and the base error between the PTC gain and that calculated with the flats. We generated histograms of these parameters to examine the behavior of the vendor's data and extract general trends. To exclude outliers, i.e., CCD segments with abnormal behavior, we utilized the *sigma_clip* and *sigma_clipped_stats* functions from Astropy Collaboration et al. (2018). These functions allowed us to cut the data such that only values within 3σ of the median were retained, and we performed this operation iteratively three times to ensure robustness.

3.2.1 Simulation

The methodology outlined in Section 3.2 and the utilization of LSST software version *w_2022_27* yielded the results depicted in Figures 6 and 7. Figure 6 showcases the relative percent error between the gains for E2V sensor 55 (top panel) and ITL sensor 74 (bottom panel) over the flow range below the PTC turnoff. The embedded plot on the left displays the behavior between 5000 and 10000 ADU, along with the corresponding linear fit, while the plot on the right shows the error for each CCD segment within the same flow range. Notably, the embedded plot reveals that the relative error has an offset exceeding 5% for these two sensors, prompting us to construct a histogram with the offset values for the entire focal plane to determine if

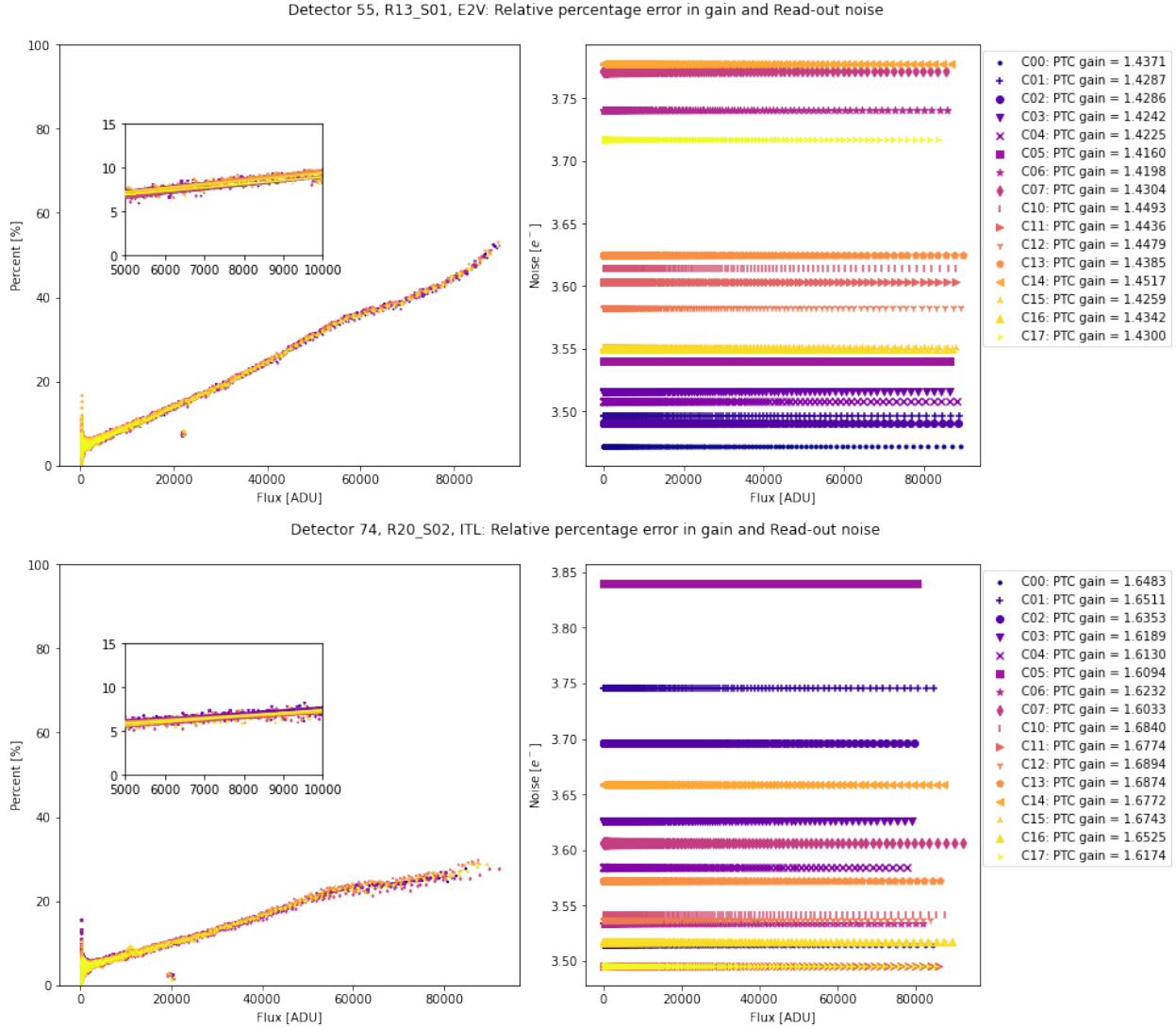


Figure 6: The relative percentage error between the gain estimated by the PTC and the gain calculated from two flat images is shown in the left panels, while the read-out noise of each amplifier is shown in the right panels. The upper panel displays the results for detector 55 (R13_S01) with vendor E2V, and the lower panel shows the results for detector 74 (R20_S02) from vendor ITL. Each color and symbol in the plots represents the relative percentage error for one of the 16 segments that make up each CCD. The embedded image in the left panels shows the percentage error specifically between 5000 and 10000 ADU, corresponding to the low flux regime where a linear fit is performed. The data used to construct these plots includes only values below the PTC turnoff.

this behavior is widespread. Figure 7 confirms that this relative error is a prevalent characteristic exhibited by all sensors, with an average base error of $\sim 5\%$, which we consider relatively

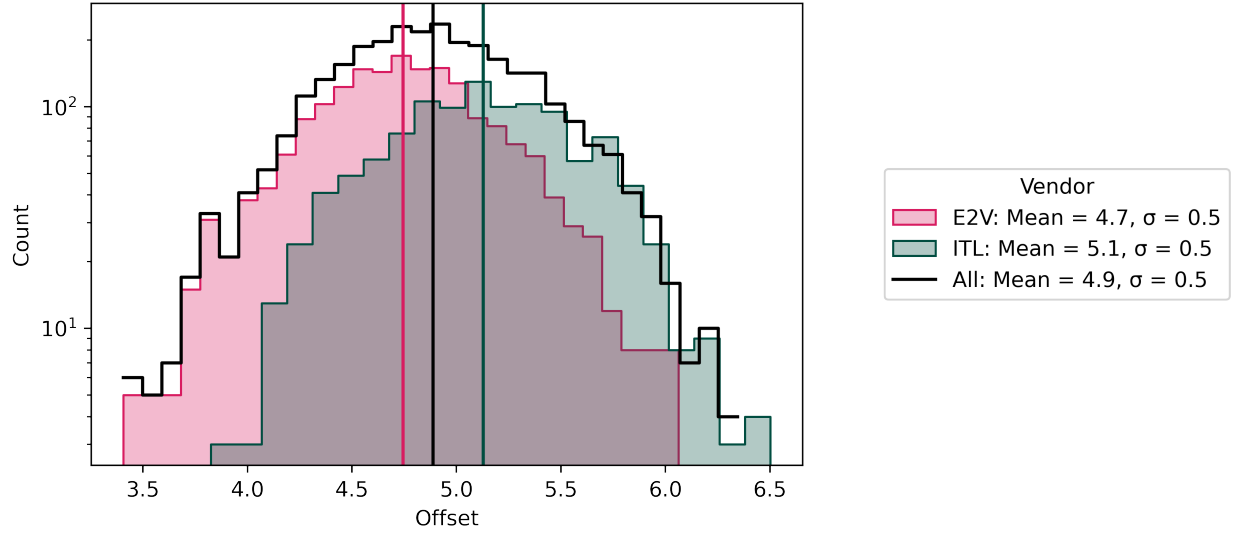


Figure 7: The histograms display the offset value obtained from the linear fit for flows between 5000 and 10000 ADU, representing the relative percentage error between gains. The magenta distribution represents the results for vendor E2V, with a mean of (4.7 ± 0.5) %. The blue distribution shows the results for vendor ITL, with a mean of (5.1 ± 0.5) %. The black distribution represents the histogram of all data without discrimination by vendor, with a mean of (4.9 ± 0.5) %. Vertical lines indicate the value of the mean for each distribution.

high. Thus, we further investigated this issue through simulations.

Various factors, including potential overestimation of the read-out noise, the influence of masks used in the images, or assumptions about the distribution for the operations between flat images as given by Equation 8, could contribute to the observed behavior. The *w_2022_27* version of the *DM stack* assumes that Equation 8 follows a Gaussian distribution.

$$\frac{(I_1 - I_2)^2}{I_1 + I_2} \quad (8)$$

To better understand and address this issue, further analysis and simulations were conducted. If the distribution is found to deviate from a Gaussian distribution, the distribution statistics would need to be modified accordingly. To explore possible variables, we conducted simulations in three different cases, as described below:

- **Case 1 - Noise Overestimation:** Two data sets were constructed following a Poisson distribution for the flow, with an expected value ranging from 5000 to 10000 ADU. In our case, we chose 5000 ADU as the expected value. The Poisson distribution is given by:

$$f(k; \lambda) = \frac{\lambda^k e^{-\lambda}}{k!} \implies f(k; 5000) = \frac{5000^k e^{-5000}}{k!} \quad (9)$$

where λ is the expected value and k is the number of events. To this data, we added Gaussian noise with a mean of zero and a dispersion value that we assume as the read-out noise, given by:

$$p(x) = \frac{1}{\sqrt{2\pi}\sigma^2} \exp\left(-\frac{(x-\mu)^2}{2\sigma^2}\right) \implies p(x) = \frac{1}{\sqrt{2\pi}N^2} \exp\left(-\frac{x^2}{2N^2}\right) \quad (10)$$

where μ is the mean, σ is the standard deviation, and N is the read-out noise that we assume. Finally, we apply the methodology described in Section 3.2 for all types of gain correction: NONE, SIMPLE, and FULL, and calculate the relative error using a base gain (chosen as 2.0) to verify if we can replicate the observations in Figure 6, specifically a base error above 5%.

- **Case 2 - Pixel Masks:** In this step, pixel masks are added to Case 1. The respective mask is extracted from each flat image, where each flat has an average of 5000 ADU counts. This mask filters out suspicious, bad, dead, and saturated pixels. Next, a Poisson distribution is generated with the dimensions of one of the CCD segments for which the masks were extracted, i.e., $size_x = 2002$ and $size_y = 512$, along with its respective Gaussian noise. The generated mask is then applied to each array using the *Numpy* function (Harris et al., 2020) *ma.masked_where*.

Case 3 - Statistics control: Building upon Case 2, we incorporate statistics control by assuming that the distribution of equation 8 follows a Gaussian distribution. Similar to the approach used in section 3.2, we truncate the distribution by keeping only the data points that fall within 5.5σ of the mean, and we repeat this process for three iterations. When the distribution of equation 8 is Gaussian, the mean of the symmetrical truncated distribution is the same as the original one, and the mean of non-symmetrical truncated distribution can be calculated as:

$$\mu = \bar{\mu} - \bar{\sigma} \frac{\phi(0, 1; \beta) - \phi(0, 1; \alpha)}{\Phi(0, 1; \beta) - \Phi(0, 1; \alpha)} ; \alpha = \frac{a - \bar{\mu}}{\bar{\sigma}}, \beta = \frac{b - \bar{\mu}}{\bar{\sigma}} \quad (11)$$

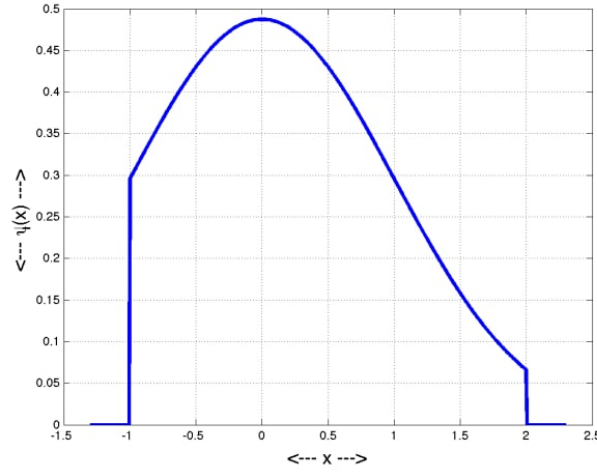


Figure 8: The truncated Gaussian distribution with a zero mean and standard deviation is represented by $\psi(0, 1, a = -1, b = +2; x)$. This figure is sourced from Burkardt (2023).

where α and β are standardized variables, a and b are the cutoff values for the lower and upper tails of the distribution, respectively, $\bar{\mu}$ and $\bar{\sigma}$ are the statistics of the original distribution, ϕ represents the normal probability density function (PDF), and Φ represents the Normal cumulative distribution function (CDF). Figure 8 illustrates this case for $a = -1$ and $b = +2$. However, when the distribution is symmetrically truncated, i.e., $-a = b$, the numerator of the second term in the above equation becomes zero, and the mean of the truncated and original distribution is simply:

$$\mu = \bar{\mu} \quad (12)$$

This implies that the mean of the truncated and original distribution are equal, as mentioned earlier. We use this result to calculate the expected value of equation 3 in order to determine the gain solutions for the NONE, SIMPLE, and FULL corrections. As an additional step, we examine the shape of the distribution of equation 8; if the distribution of equation 8 is not Gaussian, no truncation is applied, and the expected value of equation 3 is calculated using the arithmetic mean.

3.3 No linearity Correction

To study the impact of linearity correction on the PTC shape and parameters, we applied a 12-node spline linearizer to detectors 32 (ITL) and 139 (E2V). The effectiveness of this method

was established in RTN-055, where it was found that a 12-node spline significantly corrects the nonlinearity effect and reduces residual dispersion. All configurations remained unchanged, except for the linearity correction (see table 1).

Table 1: The configuration used to generate the PTCs when we include the linearity correction (the parameter 'doLinearize' is set to 'true').

Configurations			
doWrite: true	doLinearize: true	doFlat: false	doInterpolate: false
doOverscan: true	doCrosstalk: false	doFringe: false	doSaturation: false
doAssembleCcd: true	doBrighterFatter: false	doApplyGains: false	doSaturationInterpolation: false
doBias: true	doDark: true	doDefect: true	growSaturationFootprintSize: 0
doVariance: true	doStrayLight: false	doNaNMasking: true	ptcFitType: EXPAPPROXIMATION

Subsequently, plots of the ratio of Variance to Mean vs Mean are constructed, normalizing the variance. This allows for analysis of whether the bump between 50000 and 60000 ADU is corrected. Additionally, a relative percentage error between the parameters obtained from the PTC fit with and without linearity correction is calculated to quantify the effect on these parameters. Finally, a comparison is made to check if the parameters and/or the shape of the PTC changed compared to the version without correction for nonlinearity.

3.4 Crosstalk Correction

The LSSTCam's full focal plane can be read out in 2 seconds, and the combination of high-speed, high-resistivity silicon components and close spacing between each channel makes it more susceptible to electronic crosstalk compared to other mosaic cameras (O'Connor, 2015).

Electronic crosstalk occurs in CCDs with multiple channels that are read simultaneously and coupled, resulting in ghost images generated in adjacent segments when a bright source is detected in a channel due to this coupling (Snyder et al., 2020). This effect is illustrated in Figure 9, where ghost signals are observed in the lateral segments of the detector. Figure 10 shows a heat map on the left for ITL detector 32 and on the right for ITL detector 139, depicting the crosstalk coefficients in blue colors, with the observation that the crosstalk pattern differs per vendor. These coefficients are incorporated into a configuration file in the LSST software to regenerate the PTC with this correction.

Finally, similar to the approach in Section 3.3, a comparison was made to check whether the parameters and/or the shape of the PTC changed compared to the version without correction

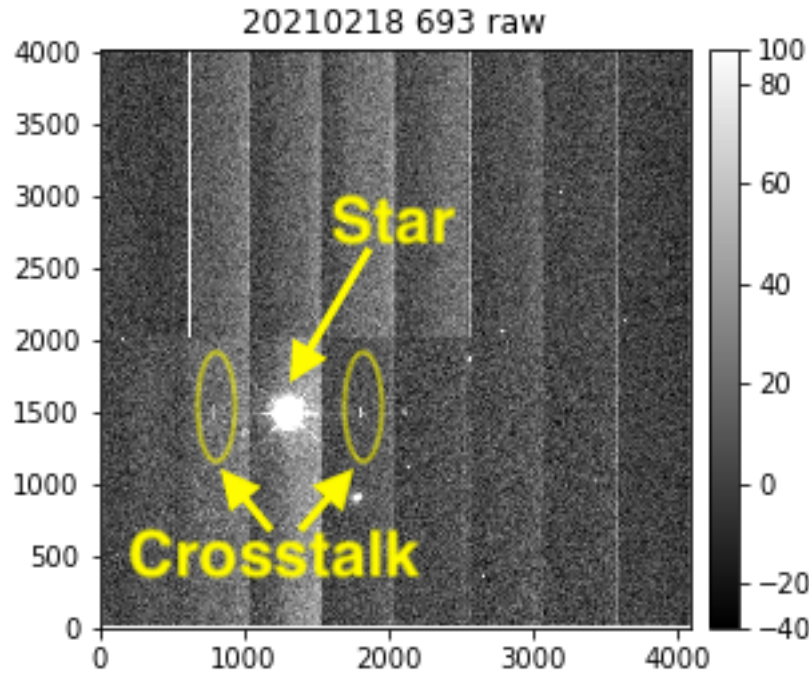


Figure 9: An image of a bright star captured with the 1.2m auxiliary telescope at the Vera Rubin Observatory, revealing crosstalk in segments adjacent to the star's image.

for crosstalk.

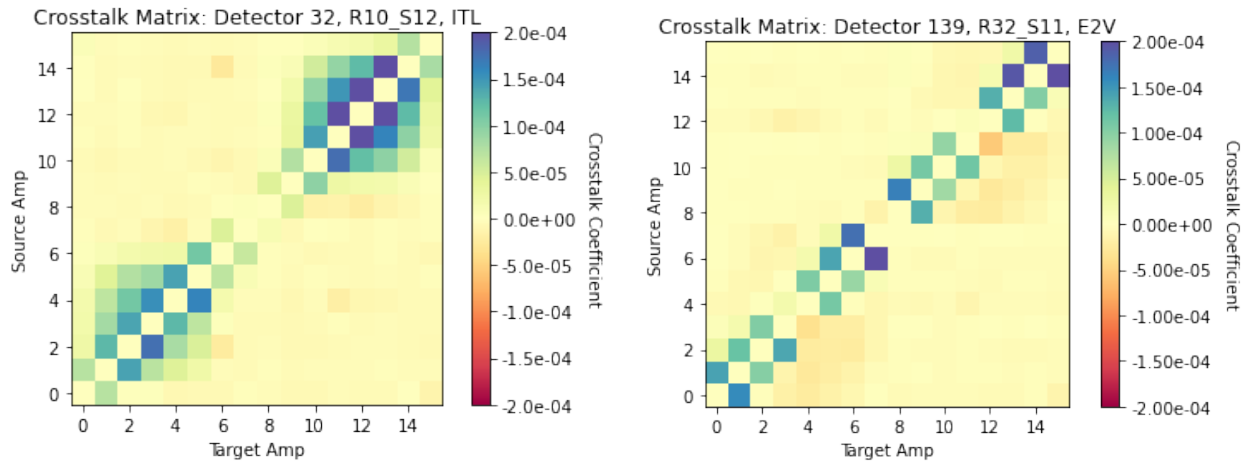


Figure 10: Crosstalk matrix shown on the left for detector 32 (ITL) and on the right for detector 139 (E2V).

4 Results

4.1 Photon Transfer Curve

As part of this project, a key initial task was to utilize the PTC to determine essential parameters for each CCD segment across the focal plane using the *DM stack*. This has already been done by SLAC National Accelerator Laboratory⁵ (referred to as SLAC hereafter) for this particular run (SLAC heat maps BOT 13144), and we aim to reproduce their results in this study.

Initially, PTCs were generated by CCD for the entire focal plane, as shown in Figure 11, to detect any abnormal behavior and low PTC-turnoff values (below 40000 ADU). Detectors found with low PTC-turnoff and/or misclassified were recorded in Table 2. Furthermore, a visual inspection revealed that approximately 60 % of the detectors had at least one segment exhibiting a *Downing dip*.

Subsequently, heat maps were generated for the entire focal plane, similar to those performed by SLAC, as shown in the panels of Figure 12, to visualize the parameters estimated by fitting the PTC: gain and read noise in the upper left and right panels, respectively, and a_{00} and turnoff in the lower left and right panels, respectively. Notably, bimodality is observed in the gain and a_{00} values, which account for the BF effect. The more reddish values dominate in the E2V sensors, while the more yellow values dominate in ITL sensors, indicating that E2V vendor's detectors generally have a lower gain but more negative BF effect coefficients compared to ITL. In contrast, no significant effect is exhibited due to the vendor for readout noise and turnoff.

The histograms in Figure 13 support the behavior described above by the heat maps, revealing clear bimodality for gain and a_{00} , and a more generalized behavior for read noise and turnoff. The average gain values for E2V sensors are $1.49 \pm 0.05 \text{ } e^-/ADU$, and for ITL sensors are $1.69 \pm 0.05 \text{ } e^-/ADU$. The average BF effect coefficient values are $(-3.0 \pm 0.1) \times 10^{-6}$ for E2V and $(-1.7 \pm 0.2) \times 10^{-6}$ for ITL.

Although the results of this work are generally congruent with those obtained by SLAC, some differences were found in certain segments, particularly for gain values in segments C04 and C14 of detector 0 (R01_S00), C00 of detector 22 (R03_S11), and C02 of detector 169 (R41_S21). Table 2 highlights these segments in red, where the most notable differences between our

⁵The code used by SLAC is available at SLAC code

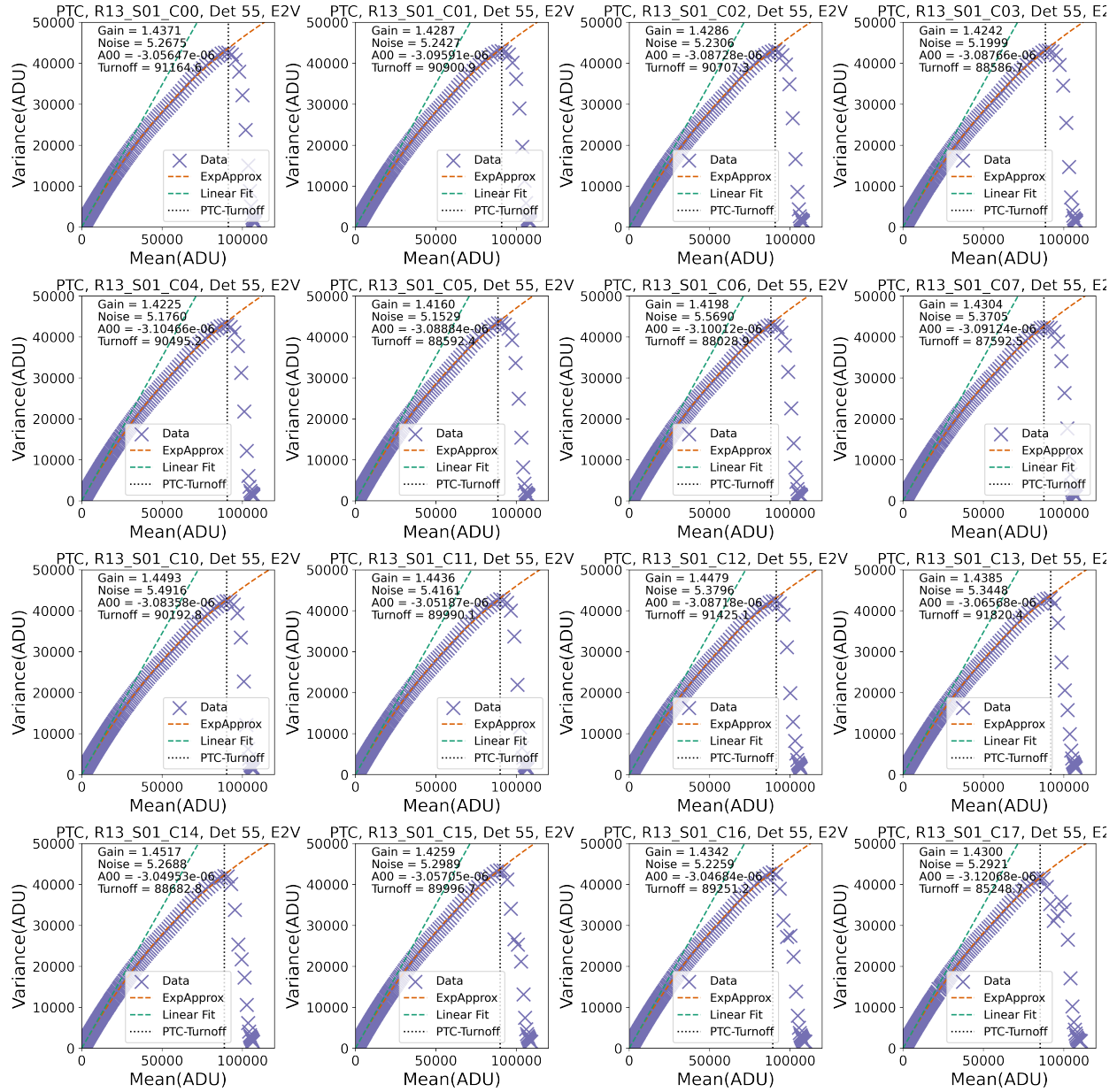


Figure 11: PTC for all segments of sensor 55 (E2V). The Xs represent the data points, the red line is the exponential fit to the PTC using the Astier16 approximation (eq. 1), and the green line is a linear fit. The obtained fit parameters include the gain, the a_{00} parameter, the PTC turnoff (Max ADU), and the read noise.

results and those of SLAC were observed for the four parameters (gain, BF coefficient, read noise, and turnoff). For detector 22, the values on the table suggest that the detector may possibly be dead, while for the segment of detector 169, there may be a misclassification by the

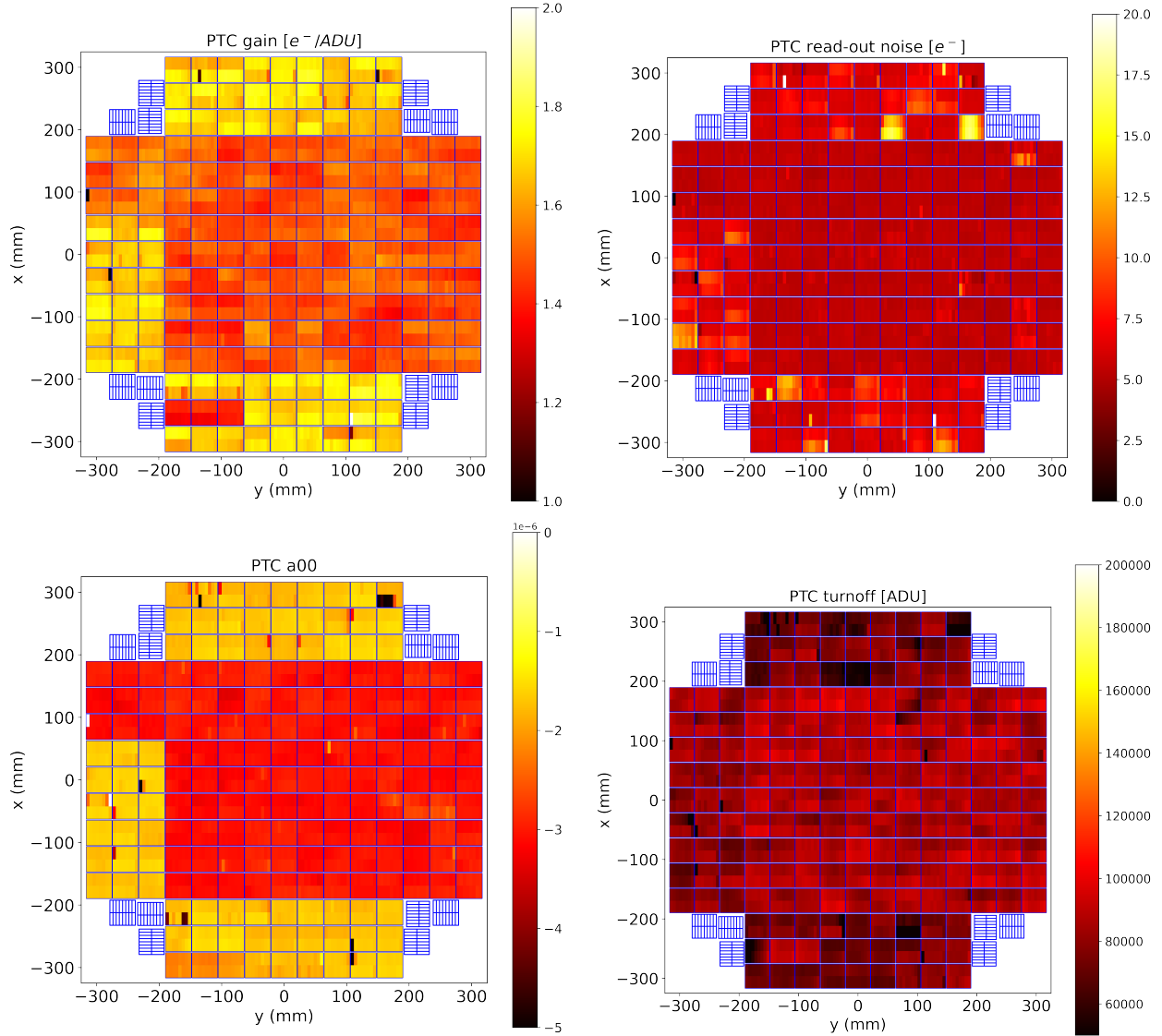


Figure 12: Heatmaps depicting the parameters obtained by fitting the PTC for each segment of the sensors across the entire focal plane. The upper panel shows the gain values on the left and the read noise on the right. The lower panel shows the values of a_{00} , which are of the order of -1×10^{-6} , on the left, and the turnoff on the right. These maps are a reproduction of those previously constructed by SLAC for the same run 13144 (SLAC heat maps).

PTC-turnoff location algorithm. These specific cases could be the reason for the differences between our results and those of SLAC. However, to determine the precise cause of these differences, a detailed analysis of the respective codes used and their versions is necessary. Discrepancies between the algorithms could arise from various factors, such as differences in the pixels used for calculation due to masks applied, variations in the image reduction tech-

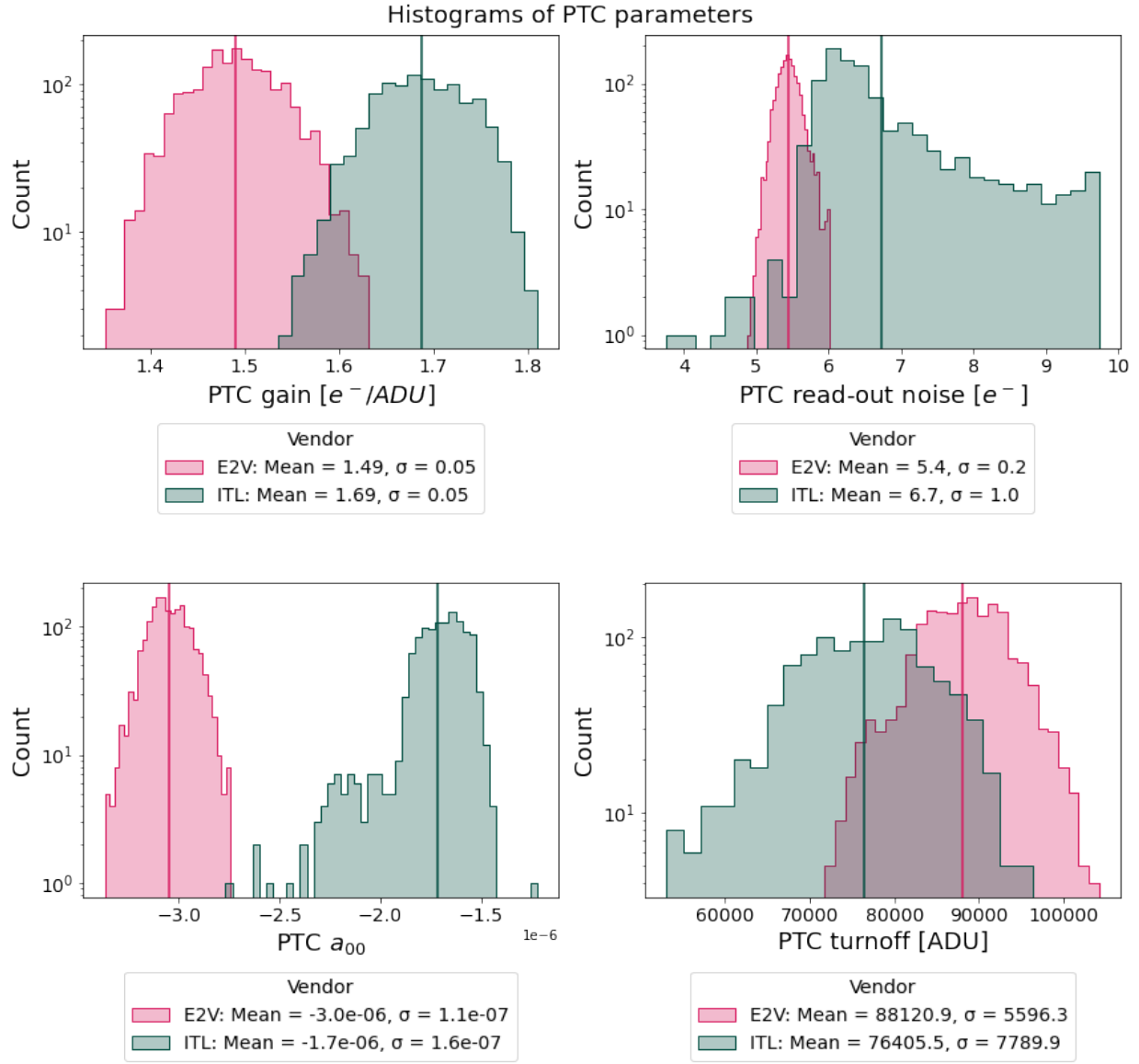


Figure 13: Histograms showing the distribution of parameters obtained from the fit to the PTC: gain (top left), read noise (top right), a_{00} (bottom left), and turnoff (bottom right). The distributions are shown separately for each vendor, with magenta representing E2V and blue representing ITL. The vertical lines indicate the mean value of each distribution.

niques (e.g., Instrument Signature Removal or ISR), or differences in the rejection of outliers, among others. Further investigation is needed to elucidate the exact source of these discrepancies as we utilized the same run (13144) as SLAC.

```
206         # Cannot assume that the mean values are sorted
207         ptc_turnoff = max(mean[index])
```

(a) Eotest code

```
839         # Discard points when the variance starts to decrease after two
840         # consecutive signal levels
841         goodPoints = self._getInitialGoodPoints(meanVecOriginal, varVecOriginal,
842                                                 self.config.minVarPivotSearch,
843                                                 self.config.consecutivePointsVarDecreases)
844
857         # Save the point where the variance starts decreasing as the
858         # PTC turnoff point
859         ptcTurnoff = meanVecOriginal[goodPoints][-1]
860         dataset.ptcTurnoff[ampName] = ptcTurnoff
```

(b) DM stack code

Figure 14: Codes used to calculate the PTC-turnoff in eotest (a), employed by SLAC, and DM stack (b), the official code for LSST data.

Overall, we observed similar behavior for the turn-off of the sensors between our work and SLAC, although the methods used for determination were different, as shown in Figure 14. In *eotest*, the PTC-turnoff is defined as the point where the variance is maximum, determined among the data whose residuals are below 5σ . On the other hand, in *DM stack*, the PTC-turnoff is defined as the point where the variance starts to decrease monotonically by at least two points (the number of points to decrease can be modified in the function `_getInitialGoodPoints`). Tests performed at SLAC National Accelerator Laboratory before the writing of this report (Aug 2022) indicate a full well value of 90000 e^- (private communication with the LSST-Cam Team at the time of writing). In contrast, our work found an average turn-off value of 83240 ADU , which corresponds to an approximate FWC of $130000 \pm 10000\text{ e}^-$.

Table 2: Detectors with segments exhibiting low PTC-turnoff values (below 40000 ADU), misclassified PTC-turnoff by the algorithm, bad segments, or discrepancies compared to results obtained by SLAC (parameters highlighted in red). The table presents the detector ID (col1), detector number (col2), vendor (col3), affected segment (col4), PTC parameters (gain, BF effect, and turnoff coefficient; cols 5, 6, 7, and 8, respectively), and detected problem (col9).

Detector ID	Det Num	Vendor	Amp	Gain [e ⁻ /ADU]	Read Noise [e ⁻]	A ₀₀	Turnoff [ADU]	Issue
R01_S00	0	ITL	C04	1.5833	6.2061	-2.0160 × 10 ⁻⁶	73461.2	SLAC diff
R01_S00	0	ITL	C14	1.7514	6.4150	-2.1907 × 10 ⁻⁶	68032.3	SLAC diff
R01_S20	6	ITL	C00	1.5354	11.1174	-4.1734 × 10 ⁻⁶	65371.7	SLAC diff
R01_S20	6	ITL	C05	1.4837	15.5104	-4.5175 × 10 ⁻⁶	76106.5	SLAC diff
R01_S20	6	ITL	C06	1.5104	13.5644	-4.3955 × 10 ⁻⁶	72293.9	SLAC diff
R02_S20	15	ITL	C17	1.67191	5.81973	-2.20396 × 10 ⁻⁶	30567.4	low PTC-turnoff
R03_S11	22	ITL	C00	15.2117	44.0087	-0.708105	223.072	SLAC diff - dead?
R10_S11	31	ITL	C10	1.63413	4.13177	-3.65785 × 10 ⁻⁶	32842.4	low PTC-turnoff
R20_S00	72	ITL	C17	0	0	nan	0	SLAC diff and dead
R20_S01	73	ITL	C00	1.6083	6.45279	-3.12539 × 10 ⁻⁶	35507.4	low PTC-turnoff
R20_S12	77	ITL	C00	1.59232	4.70427	-8.02249 × 10 ⁻⁶	26827.1	low PTC-turnoff
R30_S00	117	E2V	C10	0	0	nan	0	SLAC diff and dead
R41_S20	168	ITL	C16	1.61074	6.07818	-1.98753 × 10 ⁻⁶	37863.2	low PTC-turnoff
R41_S20	168	ITL	C17	1.59228	9.57256	-2.54637 × 10 ⁻⁶	26120	low PTC-turnoff
R41_S21	169	ITL	C02	1.08095	62.8775	-4.52943 × 10 ⁻⁶	16237.9	SLAC diff and PTC-turnoff mismatch
R41_S21	169	ITL	C11	1.61255	5.23312	-2.61051 × 10 ⁻⁶	32467.3	PTC-turnoff mismatch
R41_S21	169	ITL	C15	1.59804	5.21757	-2.31531 × 10 ⁻⁶	39151.3	PTC-turnoff mismatch
R41_S22	170	ITL	C10	1.60171	4.76741	-3.2105 × 10 ⁻⁶	32369.9	low PTC-turnoff
R42_S00	171	ITL	C17	1.6516	6.4254	-3.09362 × 10 ⁻⁶	30253.3	low PTC-turnoff
R43_S10	183	ITL	C17	1.59721	8.53352	-2.46596 × 10 ⁻⁶	30195.2	low PTC-turnoff
R43_S22	188	ITL	C00	1.6348	5.28826	-4.64678 × 10 ⁻⁶	21477.5	SLAC diff
R43_S22	188	ITL	C01	1.6348	5.28826	-4.64678 × 10 ⁻⁶	21477.5	low PTC-turnoff
R43_S22	188	ITL	C02	1.55382	6.94625	-7.40255 × 10 ⁻⁶	30764.3	low PTC-turnoff
R43_S22	188	ITL	C03	1.56826	7.24918	-4.92713 × 10 ⁻⁶	38222.4	low PTC-turnoff
R43_S22	188	ITL	C04	1.58147	3.76291	-4.88158 × 10 ⁻⁶	38143.6	low PTC-turnoff

4.2 Gain from Flat Pairs

Initially, we utilized the PTC method to obtain the gain values. However, this approach can be time-consuming as it requires fitting over a wide range of flux values. Therefore, we explored an alternative method, which we refer to as the *gain by pairs of flats*, that is less time-intensive. The left panel of Figure 15 displays the gain values for detector 55 in a flux range of 0 to ~ 120000 ADU, including values that exceed the saturation level marked by the vertical lines indicating the PTC-turnoff for each segment. On the right panel, the gain values are slightly further from the saturation level, revealing a bump around 60000 ADU due to nonlinearity, which will be discussed in Section 4.3. It is important to note that for the analysis of the gain per pair of flats, we only use data below the PTC-turnoff.

In this section, we highlight the differences we observed between the gain obtained from the PTC and pairs of flats, explore possible ways to reduce these differences, and discuss what can be expected from this alternative method in comparison to the first one.

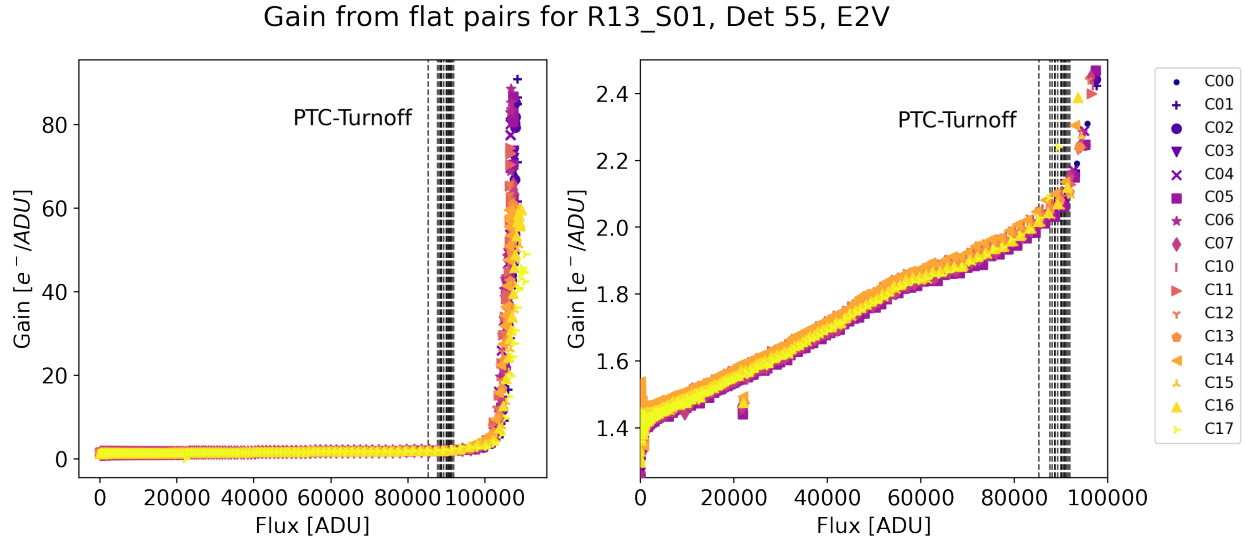
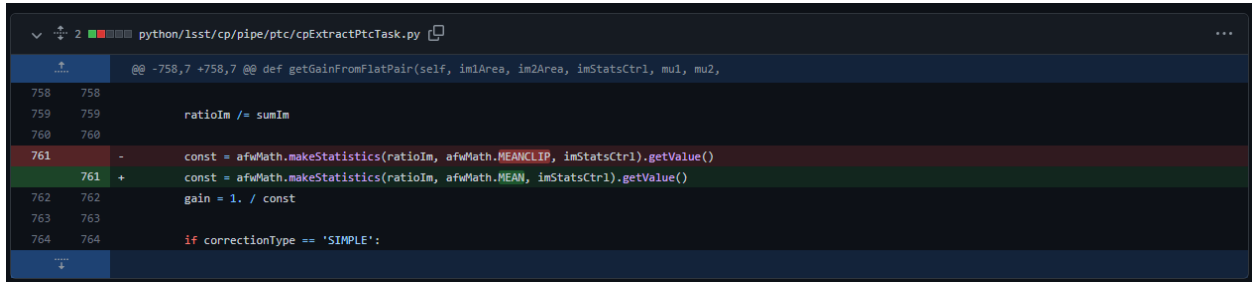


Figure 15: Gain values obtained from pairs of flat exposures for fluxes up to approximately 120000 ADU for detector 55 (R13_S01). In both panels, the dashed vertical lines indicate the PTC turnoff values for each of the 16 detector segments, while the colored data points represent the gain as a function of the flux values for each segment. The right panel zooms in on the region up to the PTC-turnoff point shown in the left panel.

As mentioned in the methodology (sec. 3), we used two code versions (w_2022_27 and w_2022_32), with the main difference and our focus shown in figure 16. This figure illustrates how the two

code versions handle statistics to compute gain from pairs of flats. The `w_2022_27` version (shown in red) assumes a Gaussian distribution and truncates the distribution to reject outliers, while the `w_2022_32` version (shown in green) rejects this assumption. Based on our analysis results described in this section, we recommend using the `w_2022_32` version, as the distribution of the operation between two flat images, which is used to calculate the gain, does not follow a Gaussian distribution. Truncating the distribution can alter the expected value for the gain.



```
python/lsst/cp/pipe/ptc/cpExtractPtcTask.py
@@ -758,7 +758,7 @@ def getGainFromFlatPair(self, im1Area, im2Area, imStatsCtrl, mu1, mu2,
758 758
759 759     ratioIm /= sumIm
760 760
761 -     const = afwMath.makeStatistics(ratioIm, afwMath.MEANCLIP, imStatsCtrl.getValue())
761 +     const = afwMath.makeStatistics(ratioIm, afwMath.MEAN, imStatsCtrl.getValue())
762 762     gain = 1. / const
763 763
764 764     if correctionType == 'SIMPLE':
```

Figure 16: Difference between the initial code (`w_2022_27`, shown in red) and current code (`w_2022_32`, shown in green) for calculating the gain from a pair of flat fields.

The version `w_2022_27` yielded unexpected results, as shown in figure 6, where the relative percentage error between the gain per PTC and flat pair exceeded 5% at a flux of 5000 ADU. This was observed for both E2V (upper panel) and ITL (lower panel) detectors. To investigate the cause of this high percentage error, simulations were performed using the methodology described in section 3.2.1.

4.2.1 Simulation

Based on the previous result of a 5% relative error between gains at 5000 ADU, we formulated several hypotheses. Firstly, we considered the possibility that the masks in the flat images could be causing the error, such as if the masks of each image are significantly different and the code uses them for calculations. Secondly, we considered the potential overestimation of read noise. Lastly, we investigated other statistical factors that could be contributing to the error.

To explore these hypotheses, we conducted simulations using a flat image of a CCD segment and actual segment masks. The use of one mask for both flats, the union of both masks, or different masks for each flat did not account for the observed 5% error at 5000 ADU, as shown in the top panel of Figure 17. Interestingly, we observed that higher read noise, when using a

NONE type correction, resulted in larger discrepancies between the expected and calculated gain ($2 e^-/\text{ADU}$). However, subsequent corrections (SIMPLE and FULL), which account for the read noise, accurately calculated the expected gain value. Nevertheless, the bottom panel of the figure, which includes control statistics in addition to the masks, consistently showed a relative percentage error between the gain per PTC and flat pairs above 5% in all the cases. We further verify this with real data in the next section (4.2.2).

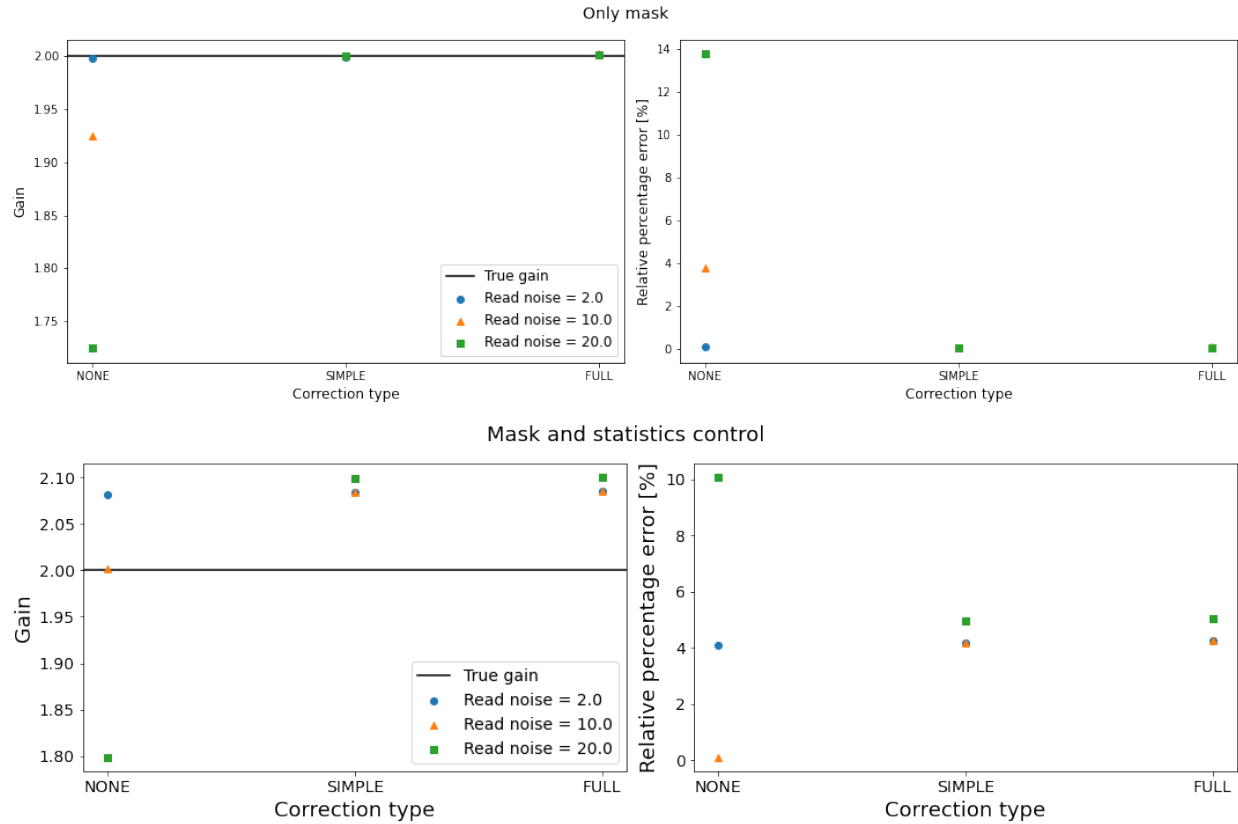


Figure 17: Simulation results for flat pair gain estimation, shown in the top panel using only masks and in the bottom panel with the addition of control statistics. The average flux value for the simulated flats is approximately 5000. The left panels display the gain values for three different models, while the right panels show the relative percentage error compared to the expected gain value of $2 e^-/\text{ADU}$. In the left panels, the horizontal black line represents the expected gain value, and the symbols denote various read noise values: blue circles for $2 e^-$, orange triangles for $10 e^-$, and green squares for $20 e^-$. The gain was calculated for three models: NONE, SIMPLE, and FULL, taking these read noise values into account.

4.2.2 Contrasting the simulations with real data

We verified the results obtained from the simulations by comparing them with actual data, specifically for detector 55 (R13_S01) and all its segments, as shown in figures 18 and 19. In these figures, the black crosses represent the gain values obtained from the PTC. The first figure confirms that the use of masks without control statistics results in a relative error of no more than 5% for any segment of the detector. The highest error observed is 2.25% at an average flux of 5450 ADU, and the same mask was used for all calculations, i.e., the union of the individual masks. On the other hand, the second figure, which incorporates control statistics along with the masks, reveals that handling the statistics introduces significant discrepancies between the gain values obtained from the PTC and the pairs of flats. In fact, the differences can be as high as 9% in one of the segments at an average flux of 5450 ADU. These results are consistent with the simulations.

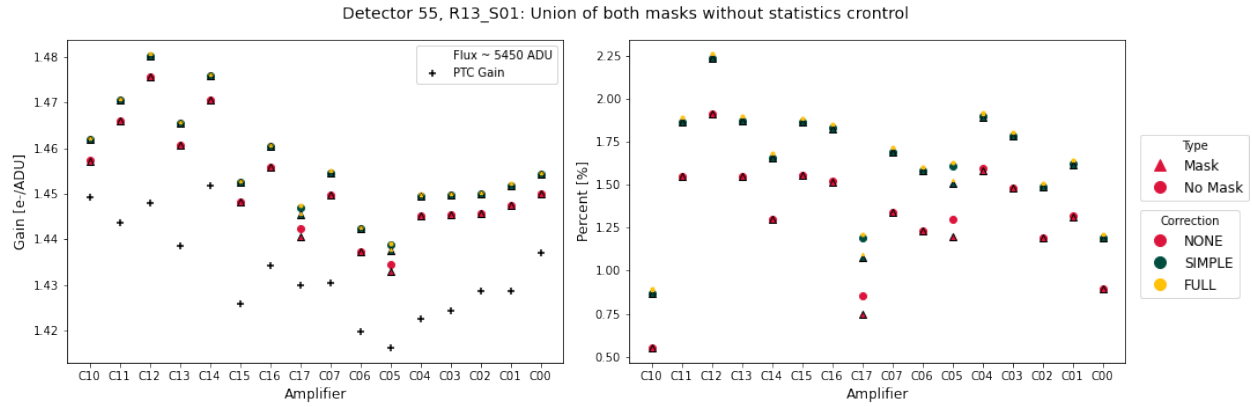


Figure 18: Gain values are shown in the left panel, while the relative percentage error is shown in the right panel, for the 16 segments (amplifiers) of detector 55 (R13_S01). In the left panel, the black crosses represent the gain values obtained from PTC. The figures in both panels indicate whether the calculation of the gain from flat pairs used masks (triangles) or not (circles), and the colors are associated with the model used to determine the gain: NONE (red), SIMPLE (green), and FULL (yellow). The mask used for calculation was the union of the masks of both flat images per segment, and control statistics were not used.

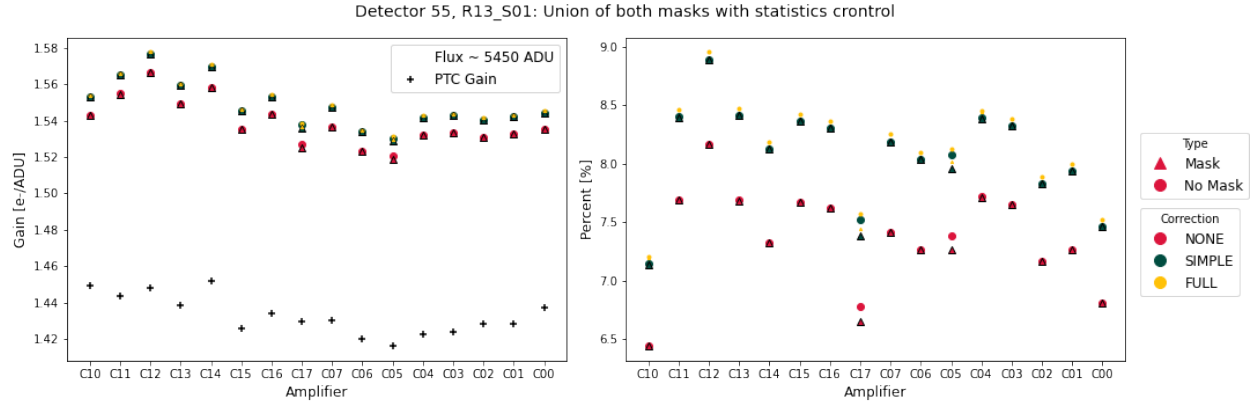


Figure 19: See description of the figure 18. This figure used control statistics.

Next, we generated plots of the distributions for the operation between the flat images using Equation 8, which is the argument of the Lupton equation (Equation 3) and directly related to the gain. The results are shown in Figure 20 for each segment of the detector, revealing that the shape of this distribution is not Gaussian. As a result, truncating this distribution can lead to a change in the mean value, which no longer coincides with the mean of the original distribution, resulting in a different gain value than expected.

Subsequently, we constructed the relative percentage error figures for the gain without truncating the distribution, as shown by the green curve in Figure 16. The resulting plot is shown in Figure 21, where the embedded image indicates that for a flux of 5000 ADU, the difference between the two gains is now below 5%, as confirmed by the simulations. Using this result, we estimated a general relationship for the gain, taking into account the distributions of the linear fit parameters, as shown in Figure 22. The linear fit was performed between 5000 and 10000 ADU. In the top left panel of this figure, we can see the distribution of slopes by vendor, revealing a clear bimodality, with E2V detectors having a slightly higher slope compared to ITL, with mean values of (0.00046 ± 0.00004) and (0.00027 ± 0.00004) % ADU, respectively. In the bottom panel of this figure, we have the intercept with the y -axis (i.e., the percentage error axis between the gains), which shows an overall mean across the detectors with no appreciable distinction by vendor, having a value of (-0.5 ± 0.5) %. Thus, the relative percentage error between 5000 and 10000 ADU for each vendor is given by:

- E2V: $Error_{2Gain} = (0.00046 \pm 0.00004)F - (0.5 \pm 0.5)$, where the error interval is $(1.8 \pm 0.7, 4.1 \pm 0.9)$ %.

- ITL: $Error_{2Gain} = (0.00027 \pm 0.00004)F - (0.5 \pm 0.5)$, where the error interval is $(0.85 \pm 0.7, 2.2 \pm 0.9) \%$.

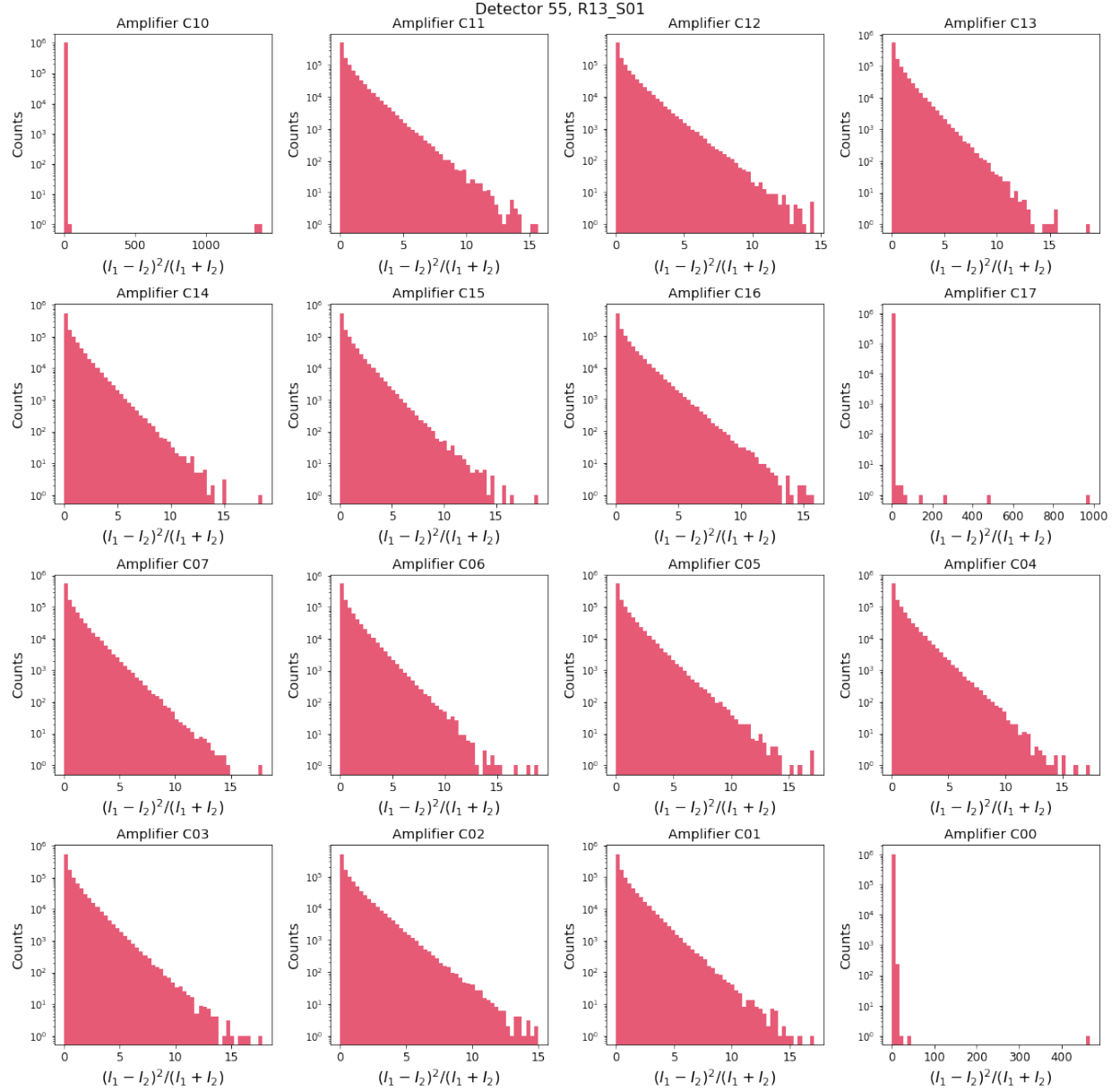


Figure 20: Histogram of the distribution for $\frac{(I_1 - I_2)^2}{I_1 + I_2}$ for each segment of detector 55 (R13_S01).

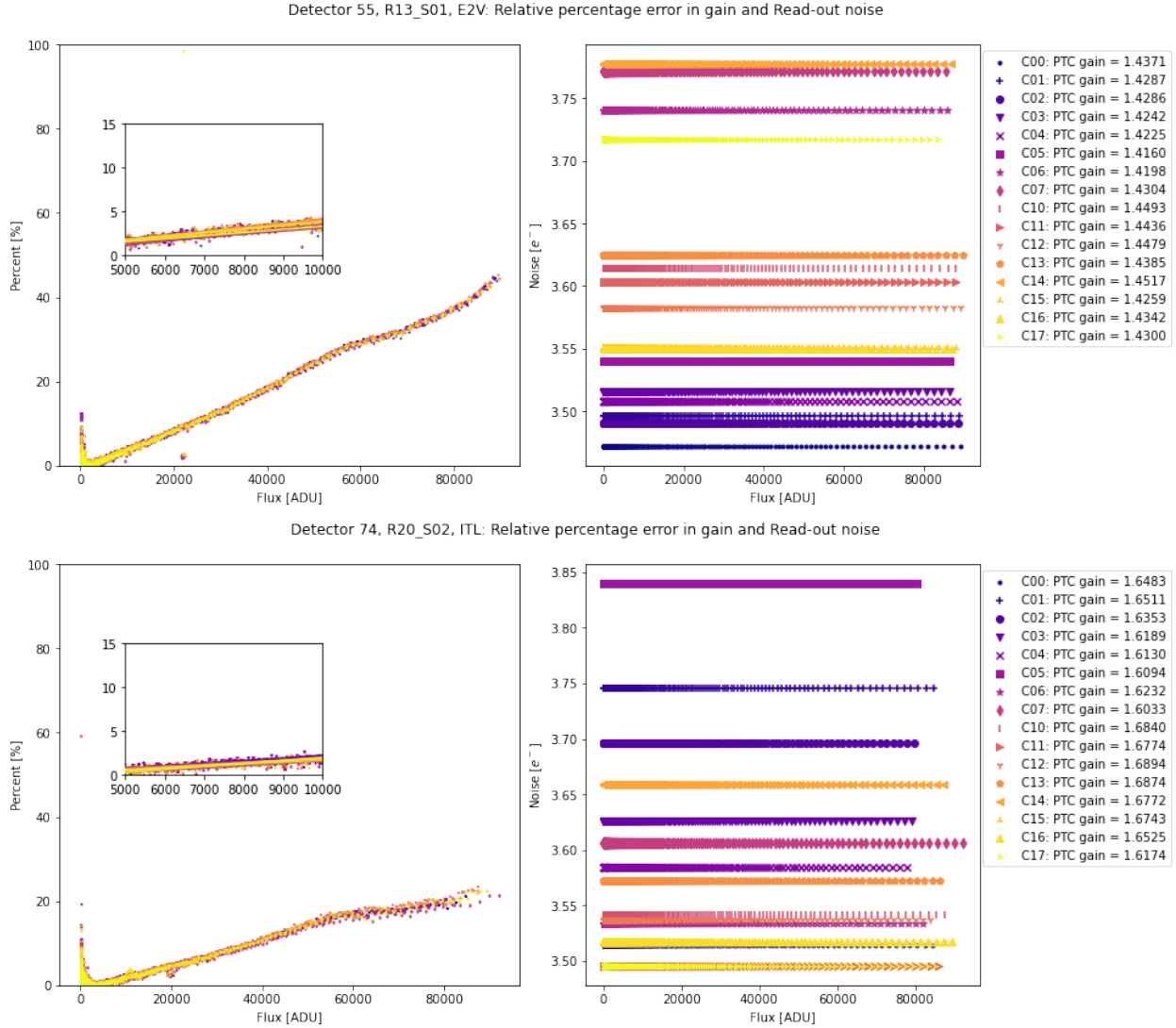


Figure 21: Refer to the description of the figure 6. This plot showcases the improved version of the code (version w_2022_32) that no longer utilizes a clipped mean

4.3 Crosstalk and Nonlinearity Correction

As part of our final analyses during this internship, we quantified and assessed whether the crosstalk effect and nonlinearity impact the shape of the PTC and/or the fundamental parameters such as gain, read noise, BF effect, and turnoff coefficient.

As described in Section 3.4, we had access to the crosstalk matrices for detector 32 (ITL) and

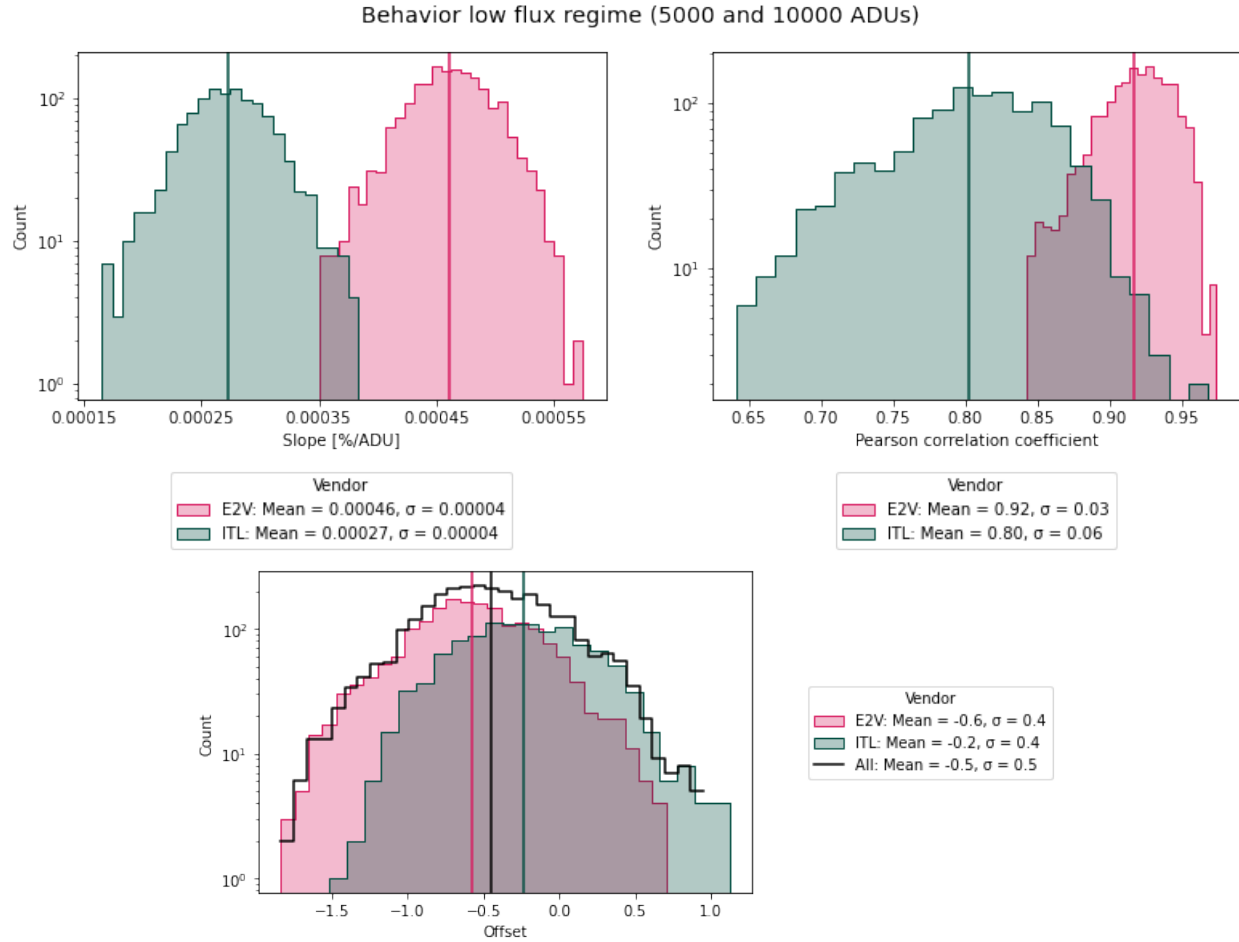


Figure 22: Histograms of the slope (top left), Pearson's correlation coefficient (top right), and y -axis intercept (offset, bottom panel) for the linear fit performed in the flow region between 5000 and 10000 ADU for the gain. The construction of these histograms utilized the updated code (version w_2022_32), and the vendor is indicated by the colors, with E2V in red and ITL in blue. The vertical lines represent the mean value for each case.

139 (E2V), which are shown in Figure 10. Applying the methodology of that section, we found that the differences between PTCs with and without crosstalk correction are negligible, as shown in Figure 23 and Figure 24. These figures illustrate that the variance differences are consistently below 0.1 ADU when considering the region below saturation. In contrast, the most significant variance in the parameters is approximately $\sim 0.1\%$ for read noise and BF effect coefficient, and approximately $\sim 0.07\%$ for gain and turnoff. The most significant differences were found in the ITL detector segments. Based on these findings, we conclude that crosstalk does not have a considerable effect on the parameters, and correcting this effect is unnecessary, as it does not alter the shape of the PTC.

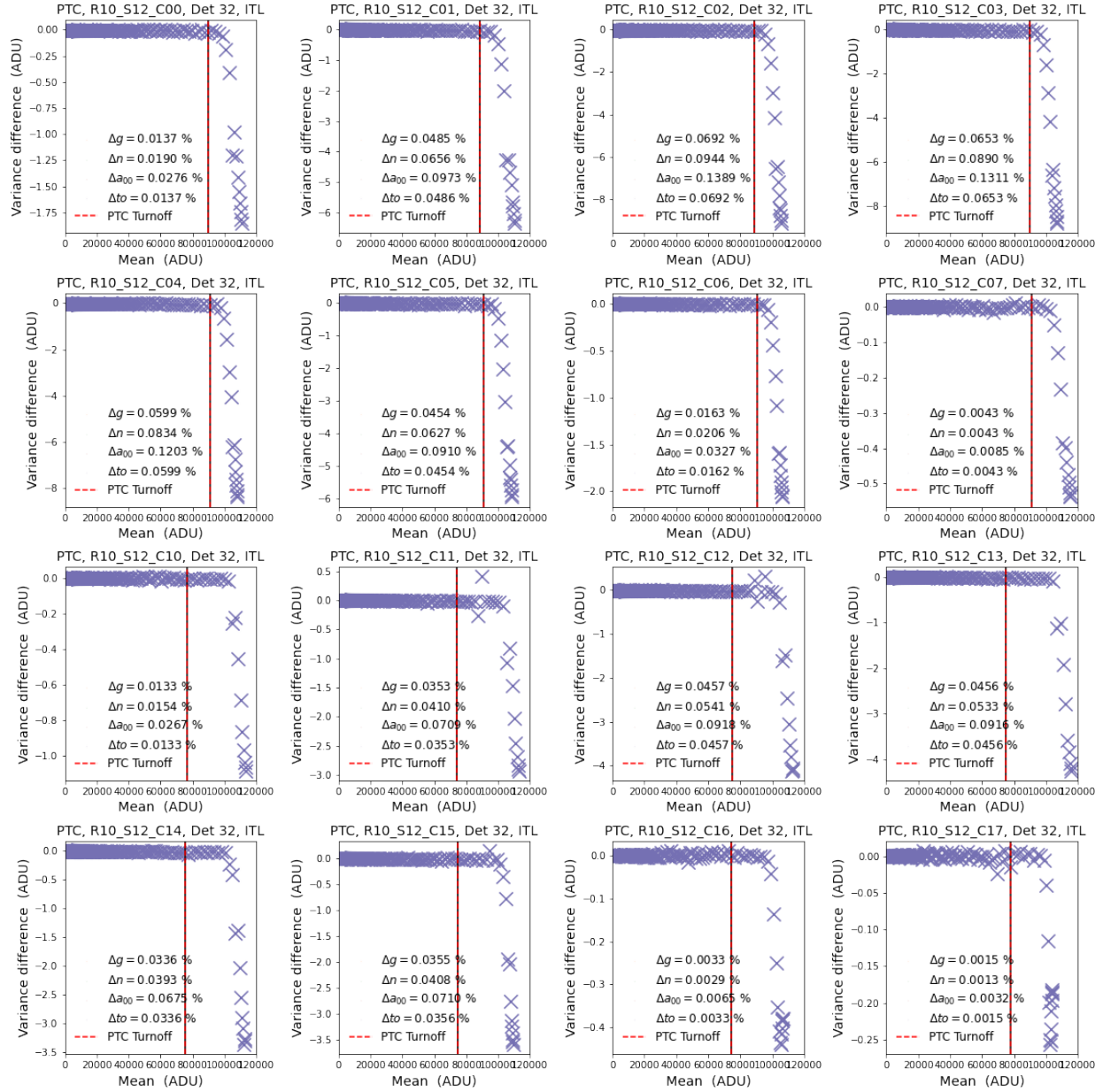


Figure 23: The plot displays the variance difference versus the mean for detector 32 (R10_S12) from vendor ITL, with the variance difference calculated between the variance values without and with crosstalk correction. Each CCD segment is shown, with vertical lines indicating the PTC-turnoff values. The legends show the parameter differences: Δg for gain, Δn for read noise, Δa_{00} for the BF effect coefficient, and Δto for the PTC-turnoff.

Finally, to verify the impact of the 12-node cubic spline linearizer on the PTC shape, we applied it to the data. The results of correcting only for crosstalk (orange dots), only for nonlinearity (blue diamonds), correcting for both effects (gray triangles), and using uncorrected data (ma-

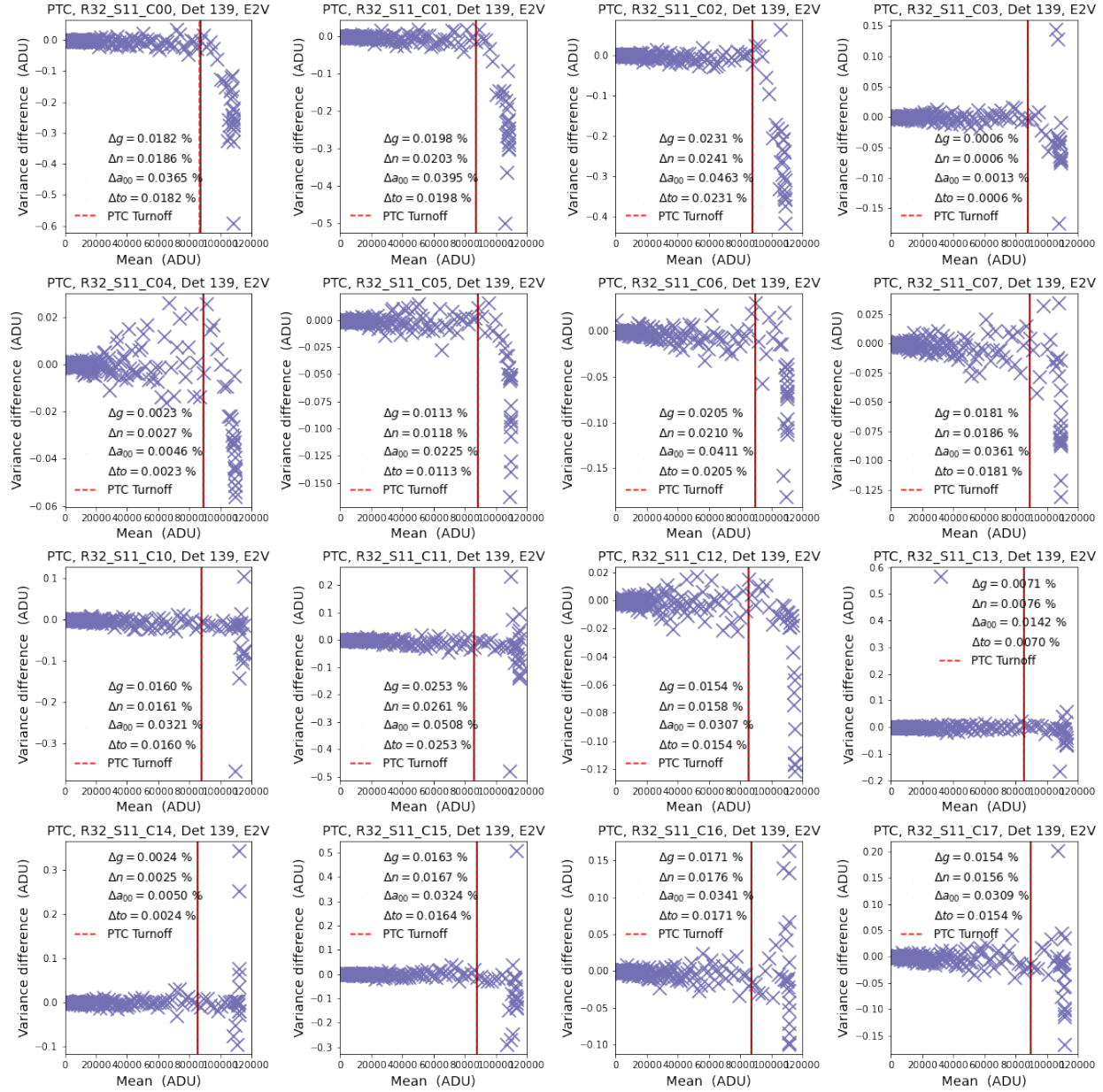


Figure 24: Refer to the description of the figure 23. This plot is for detector 139 (R32_S11) for vendor E2V.

genta squares) are presented in Figure 25. We observe that the uncorrected data show a bump around 60000 ADU, while the crosstalk-corrected data consistently align with the uncorrected data (also showing the bump), and the data corrected for nonlinearity flatten it. This suggests that making corrections for nonlinearity alone has a more significant impact on the data than making both crosstalk and nonlinearity corrections. Once again, we conclude that

crosstalk correction is not necessary as it does not affect the shape or parameters of the PTC.

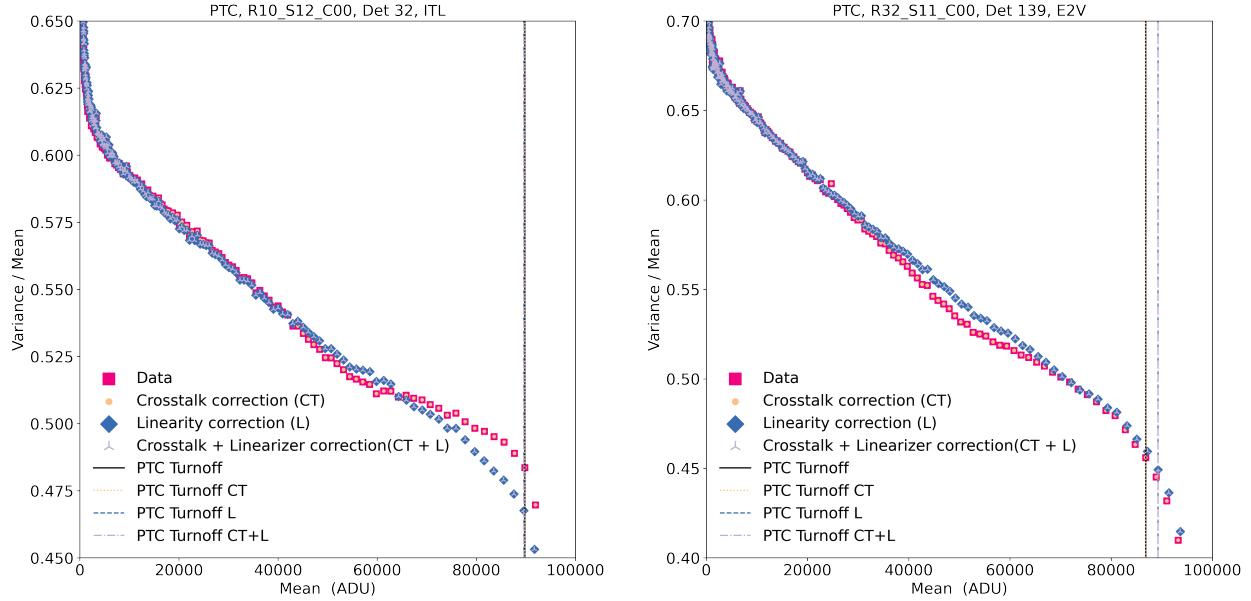


Figure 25: Variance normalized by mean vs. mean for detector 32 (R10_S12) for vendor ITL (left) and detector 139 (R32_S11) for vendor E2V (right). Data with no correction for crosstalk and nonlinearity is shown in magenta squares. Data corrected for crosstalk is shown with orange dots, while data corrected for nonlinearity is shown with blue diamonds. Triangles represent data with corrections for both crosstalk and nonlinearity. Vertical lines indicate the location of the turnoff.

5 Conclusions

In this report, we have presented a list of sensors that exhibit differences in parameters compared to those obtained by SLAC, including a PTC with low turnoff and inadequate classification. We used the default value to determine turnoff via the *DM stack*, which indicates a decrease of at least 2 points to indicate shutdown.

Our PTC study revealed a bimodal distribution per vendor for gain and a_{00} , and a more generalized behavior for read noise and turnoff. The average gain values we obtained for E2V sensors were 1.49 ± 0.05 and for ITL were 1.69 ± 0.05 e^-/ADU . The coefficient of the BF effect had an average value of $(-3.0 \pm 0.1) \times 10^{-6}$ for E2V and $(-1.7 \pm 0.2) \times 10^{-6}$ for ITL, respectively. Additionally, ITL detectors exhibited higher read noise dispersion compared to E2V, with values of 6.7 ± 1.0 e^- and 5.4 ± 0.2 e^- , respectively. These results are generally congruent with those

obtained by SLAC, although the main difference was observed in the Full Well Capacity value, with our work finding a value of $130000 \pm 10000 e^-$, while SLAC reported a value of $90000 e^-$, likely due to differences in turnoff calculation methods between *eotest* and *DM stack*.

Further analysis of the gain obtained from a pair of flats and the gain obtained from the PTC initially revealed a relative percentage error for low fluxes (5K and 10K ADU) higher than 5%. This prompted a thorough investigation, which revealed that the distribution following the Lupton equation for flat images is not of Gaussian type, leading to truncation of the distribution for statistics calculation, resulting in a shift of the mean value and consequently larger values of gain compared to the PTC gain. To address this, we performed the gain calculation without truncation and obtained percentage differences between these two gains of $(1.8 \pm 0.7, 4.1 \pm 0.9)$ for E2V and $(0.85 \pm 0.7, 2.2 \pm 0.9)$ for ITL, with these intervals corresponding to a flux region between 5000 and 10000 ADU. Accordingly, the respective report was updated and the revised calculation was implemented in the main code.

Finally, we found that linearity correction effectively fixes the observed bump around 50K-60K ADU, while correction for crosstalk does not significantly affect the shape of the PTC or modify the parameters. Therefore, we recommend implementing linearity correction only.

6 Acknowledgments

I would like to express my sincere gratitude to the entire RECA internship program team for their vision and efforts in creating this program that has provided an invaluable opportunity for research and learning for students in Colombia. I am also grateful to LSSST Corporation for generously supporting the realization of this project.

I am deeply thankful to my advisors, Drs. Andrés M. Plazas and Craig Lage, for their guidance, mentorship, and unwavering support throughout this learning journey. Their expertise, patience, and willingness to address my questions have been instrumental in shaping the outcomes of this project. Despite the challenges of virtual collaboration, their dedication and mentorship have fostered a close relationship that I deeply appreciate.

I would also like to acknowledge my colleague Jerónimo Calderón for the engaging discussions, valuable feedback, and camaraderie during the course of this project.

Finally, I am grateful to all other individuals, including fellow researchers and collaborators, who have provided assistance, advice, and encouragement during this project. Your support has been invaluable in the completion of this work.

A References

Astier, P., Antilogus, P., Juramy, C., et al., 2019, A&A, 629, A36 (arXiv:1905.08677), doi:10.1051/0004-6361/201935508, ADS Link

Astropy Collaboration, Price-Whelan, A.M., Sipőcz, B.M., et al., 2018, AJ, 156, 123 (arXiv:1801.02634), doi:10.3847/1538-3881/aabc4f, ADS Link

Burkardt, J., 2023, *The truncated normal distribution*, Tech. rep., Department of Scientific Computing, Florida State University, URL https://people.sc.fsu.edu/~jburkardt/presentations/truncated_normal.pdf

[RTN-055], Calderón, J., 2023, *Study of the Linearity of the CCDs of the Vera C. Rubin Observatory*, Technical Note RTN-055, NSF-DOE Vera C. Rubin Observatory, URL <https://rtn-055.lsst.io/>

Coulton, W.R., Armstrong, R., Smith, K.M., Lupton, R.H., Spergel, D.N., 2018, AJ, 155, 258 (arXiv:1711.06273), doi:10.3847/1538-3881/aac08d, ADS Link

Downing, M., Baade, D., Sinclair, P., Deiries, S., Christen, F., 2006, In: Dorn, D.A., Holland, A.D. (eds.) High Energy, Optical, and Infrared Detectors for Astronomy II, vol. 6276 of Society of Photo-Optical Instrumentation Engineers (SPIE) Conference Series, 627609, doi:10.1117/12.671457, ADS Link

Harris, C.R., Millman, K.J., van der Walt, S.J., et al., 2020, Nature, 585, 357 (arXiv:2006.10256), doi:10.1038/s41586-020-2649-2, ADS Link

Ivezić, Ž., Kahn, S.M., Tyson, J.A., et al., 2019, ApJ, 873, 111 (arXiv:0805.2366), doi:10.3847/1538-4357/ab042c, ADS Link

Koren, M., 2020, An Influential Female Astronomer Is Getting Her Due, URL <https://www.lsst.org/sites/default/files/sites/default/files/docs/Vera%20Rubin's%20Well-Deserved%20Space%20Observatory%20-%20The%20Atlantic.pdf>

- Lage, C., Bradshaw, A., Tyson, J.A., 2017, *Journal of Instrumentation*, 12, C03091, doi:10.1088/1748-0221/12/03/C03091, ADS Link
- LSST Science Collaboration, Abell, P.A., Allison, J., et al., 2009, arXiv e-prints, arXiv:0912.0201 (arXiv:0912.0201), doi:10.48550/arXiv.0912.0201, ADS Link
- Lupton, R.H., 2014, *Journal of Instrumentation*, 9, C04023, doi:10.1088/1748-0221/9/04/C04023, ADS Link
- Newbry, S., Lange, T., Roodman, A., et al., 2018, In: Evans, C.J., Simard, L., Takami, H. (eds.) *Ground-based and Airborne Instrumentation for Astronomy VII*, vol. 10702 of *Society of Photo-Optical Instrumentation Engineers (SPIE) Conference Series*, 1070258, doi:10.1117/12.2314269, ADS Link
- NSF, 2020, NSF-supported observatory renamed for astronomer Vera C. Rubin, URL <https://beta.nsf.gov/news/nsf-supported-observatory-renamed-astronomer-vera>
- O'Connor, P., 2015, *Journal of Instrumentation*, 10, C05010 (arXiv:1501.04137), doi:10.1088/1748-0221/10/05/C05010, ADS Link
- Rubin, V.C., 2011, *ARA&A*, 49, 1, doi:10.1146/annurev-astro-081710-102545, ADS Link
- [PSTN-019]**, Rubin Observatory Science Pipelines Developers, 2025, *The LSST Science Pipelines Software: Optical Survey Pipeline Reduction and Analysis Environment*, Project Science Technical Note PSTN-019, NSF-DOE Vera C. Rubin Observatory, URL <https://pspn-019.lsst.io/>, doi:10.71929/rubin/2570545
- Sebag, J., Krabbendam, V., Claver, C., et al., 2006, In: Stepp, L.M. (ed.) *Ground-based and Airborne Telescopes*, vol. 6267 of *Society of Photo-Optical Instrumentation Engineers (SPIE) Conference Series*, 62671R, doi:10.1117/12.670615, ADS Link
- SLAC National Accelerator Laboratory, NSF-DOE Vera C. Rubin Observatory, 2025, *The LSST Camera (LSSTCam)*, URL <https://www.osti.gov/servlets/purl/2571927>, doi:10.71929/rubin/2571927
- Snyder, A., Barrau, A., Bradshaw, A., et al., 2020, In: Holland, A.D., Beletic, J. (eds.) *X-Ray, Optical, and Infrared Detectors for Astronomy IX*, vol. 11454 of *Society of Photo-Optical Instrumentation Engineers (SPIE) Conference Series*, 1145439, doi:10.1117/12.2562915, ADS Link
- Walter, C.W., 2015, *Journal of Instrumentation*, 10, C05015 (arXiv:1505.03639), doi:10.1088/1748-0221/10/05/C05015, ADS Link

B Acronyms

Acronym	Description
ADU	Analog-to-Digital Unit
AGN	Active Galactic Nuclei
API	Application Programming Interface
B	Byte (8 bit)
BAO	Baryonic Acoustic Oscillations
BF	Brighter Fatter
BOT	Bench for Optical Testing
BPS	Batch Processing Service
CCD	Charge-Coupled Device
CDF	Cumulative Distribution Function
DM	Data Management
E2V	Teledyne e2V
FWC	Full Well Capacity
ISR	Instrument Signature Removal
ITL	Imaging Technology Laboratories
LF	luminosity function
LSST	Legacy Survey of Space and Time (formerly Large Synoptic Survey Telescope)
LSSTCam	LSST Science Camera
NSF	National Science Foundation
PDF	Probability Density Function
PSF	Point Spread Functions
PSTN	Project Science Technical Note
PTC	Photon Transfer Curve
RECA	Red de Estudiantes Col
RTN	Rubin Technical Note
SLAC	SLAC National Accelerator Laboratory